

**CPT and  $N$ -resonance phenomena in rubidium  
vapor for small-scale atomic clocks**

A thesis presented

by

Christopher Lee Smallwood

to

The Department of Physics

in partial fulfillment of the requirements

for the degree of

Bachelor of Arts

in the subject of

Physics

Harvard University

Cambridge, Massachusetts

May 2005

©2005 by Christopher Lee Smallwood

All rights reserved.

Advisor: Dr. Ronald Walsworth

Author: Christopher Lee Smallwood

## **CPT and $N$ -resonance phenomena in rubidium vapor for small-scale atomic clocks**

### **Abstract**

We report the methods and findings of two sets of tests related to the improvement of small-scale atomic clocks. The first of these is the characterization of a vertical cavity surface emitting laser (VCSEL), an increasingly valuable clock component. We describe methods employed to tune, modulate, and lock this laser, and demonstrate the production of a coherent population trapping (CPT) resonance in rubidium vapor. We also measure laser characteristics such as line width, frequency response to temperature variation, relative intensity noise (both on and off rubidium resonance), and sideband intensity.

The second set of tests explores the characteristics of a newly discovered type of multiple-photon resonance in  $^{87}\text{Rb}$  (the  $N$ -resonance) that may be useful as an alternative to CPT in the construction of small-scale clocks. We measure light shifts, line widths, and resonance shapes in a cell containing 100 Torr of neon buffer gas. Line widths were slightly broader than a previous test of the resonance at 25 and 40 Torr of buffer gas pressure, and light shifts with respect to laser intensity increased slightly. On the other hand, light shift with respect to frequency diminished, and contrast remained good at high buffer gas pressure. This indicates that the  $N$ -resonance continues to be promising for atomic clock applications.

# Contents

<b>Acknowledgments</b>	<b>vi</b>
<b>List of Figures</b>	<b>ix</b>
<b>1 Introduction</b>	<b>1</b>
<b>2 Theory</b>	<b>5</b>
2.1 Atom-light interaction . . . . .	5
2.2 Coherent population trapping/ Electromagnetically induced transparency . . . . .	9
2.3 $N$ -resonance . . . . .	12
2.4 Resonances for clock use . . . . .	13
<b>3 VCSEL locking and characterization</b>	<b>14</b>
3.1 VCSEL properties . . . . .	15
3.1.1 Basic (unmodulated) properties . . . . .	15
3.1.2 Modulated properties . . . . .	24
3.2 Laser locking . . . . .	28
3.2.1 Experimental setup . . . . .	29
3.2.2 Locking procedures . . . . .	32

3.2.3	Locking with HF modulation . . . . .	35
3.2.4	Locking off resonance . . . . .	37
3.2.5	Ground loops . . . . .	39
3.3	EIT realization and characterization . . . . .	40
3.3.1	Procedure . . . . .	40
3.3.2	EIT observation . . . . .	41
3.4	Relative intensity noise measurements . . . . .	42
3.4.1	Theory . . . . .	42
3.4.2	RIN findings . . . . .	43
3.5	Sideband comparison measurements . . . . .	46
3.5.1	Experimental setup . . . . .	47
3.5.2	Results . . . . .	49
<b>4</b>	<b>High pressure <math>N</math>-resonance tests</b>	<b>52</b>
4.1	Characteristics of interest . . . . .	53
4.2	Experimental setup . . . . .	54
4.3	Results . . . . .	55
4.3.1	Light shifts . . . . .	56
4.3.2	Widths . . . . .	57
4.3.3	Line shape asymmetry . . . . .	58
<b>5</b>	<b>Further study</b>	<b>61</b>
<b>A</b>	<b>Technical data on the Kernco SN: 61-39 VCSEL</b>	<b>A.1</b>

## Acknowledgments

This thesis would never have come to completion, or even been attempted, had it not been for my advisor, Ron Walsworth. From as early as the fall semester of my freshman year, he has been a friendly face, and an intellectual inspiration. After I joined the group, his unwavering support, guidance, and enthusiasm have truly deepened my love of physics, and I will be forever indebted to him for that.

David Phillips and Irina Novikova have also been tremendous, and I always knew I could count on them to clear my head when nothing made sense. David never ceased to amaze me with the enthusiasm that always shined through when he explained something to me for the first time, or by the boldness with which he entrusted me to handle precious lab equipment. Irina, with her cheerfulness and patience, showed me the beauty of quantum mechanics, and taught me a tremendous amount about experimental optics.

The other members of the Walsworth Group have all helped to make this work a reality, brightening my days and making it a pleasure to come into lab. Yanhong Xiao, who took and analyzed data with me for several of the  $N$ -resonance tests, made brief comments that always made me smile, and asked hard questions that always made me think. Suzanne Rousseau shared her lab equipment, her kindness, and her copy of Audioslave, all for which I am eternally grateful. Alex Glenday helped me understand the elegance of lock loops and along with Mason Klein helped me fight the ugliness of ground loops. Leo Tsai, Federico Cane, Matt Rosen, John Ng, Tina Pavlin, Ross Mair, Ed Mattison, Marc Humphrey, and Jim Maddox were always an inspiration and often great fun during Friday lunch at the Tamarind House.

I am also indebted to Verena Martinez and Mai Mai Lin, who helped me edit the text of this thesis.

Finally, it goes without saying that I owe a great deal of thanks to my mother and brother Gregory. They are, more than anything else in the world, the two constants in my life, and I cannot begin to express my gratitude in words for their unconditional love and support.

*In memory of Tom Smallwood,  
a good clock repairman, and a great father.*

# List of Figures

2.1	Diagram of EIT in a three-level system . . . . .	9
2.2	EIT susceptibility as a function of detuning . . . . .	12
2.3	Level diagram for $N$ -resonance in a three-level system . . . . .	13
3.1	VCSEL image . . . . .	14
3.2	Preliminary VCSEL setup block diagram . . . . .	16
3.3	Kernco VCSEL circuit schematic . . . . .	18
3.4	Example data for laser sweep test . . . . .	19
3.5	Level diagram for $^{85}\text{Rb}$ and $^{87}\text{Rb}$ D1 and D2 transition lines . . . . .	20
3.6	Temperature sweep test results . . . . .	21
3.7	Concurrent signal cell and Fabry-Perot sweep . . . . .	22
3.8	Fabry-Perot verification of temperature sweep linearity . . . . .	23
3.9	Theoretical sideband diagram for high modulation index and frequency	25
3.10	High frequency modulation VCSEL setup . . . . .	26
3.11	Fabry-Perot cavity trace of high frequency sidebands at large modulation index . . . . .	28
3.12	Modulation index calculation plot . . . . .	28
3.13	VCSEL lock loop setup . . . . .	29
3.14	Theoretical absorption profile and first derivative . . . . .	30

3.15	Natural abundance Rb open-loop response . . . . .	33
3.16	Open-loop response for $^{87}\text{Rb}$ . . . . .	34
3.17	High frequency open-loop response . . . . .	36
3.18	Voltage offset-frequency detuning calibration curve . . . . .	38
3.19	VCSEL setup for observing electromagnetically induced transparency	40
3.20	EIT transmission plot . . . . .	41
3.21	PM-AM noise conversion illustration . . . . .	43
3.22	Relative intensity noise test block diagram . . . . .	44
3.23	Relative intensity noise plots . . . . .	45
3.24	Renormalized comparison of relative intensity noise calculations . . .	46
3.25	Experimental setup for sideband comparison . . . . .	47
3.26	Exmple sideband calculation data . . . . .	49
3.27	Sideband-to-carrier ratios calculated by beat note and Fabry-Perot analyses . . . . .	50
4.1	$N$ -resonance experimental setup . . . . .	54
4.2	Example absorption profiles . . . . .	56
4.3	Light shift measurements as a function of laser detuning and power .	57
4.4	Line width measurements as a function of laser power . . . . .	58
4.5	Lock-in amplifier plots as an indication of resonance shape . . . . .	59

# Chapter 1

## Introduction

Precision time measurement has been a crucial tool in physics research for some time, providing experimental confirmation of general relativity [1], allowing high-accuracy characterization of atomic structures [2], and permitting searches for Lorentz and *CPT* violation [3]. As the most accurate clocks in the world continue to improve, further applications may be explored, such as the search for evidence that the fine structure constant varies in time [4]. Accuracy and precision obtained with the best clocks are considerable. NIST-F1, a cesium fountain clock currently used as the primary time reference for the United States, displays a fractional uncertainty less than  $10^{-15}$ , remaining stable to within 1 second over the course of 30 million years [5].

Perhaps the most interesting recent developments in timekeeping have been in the miniaturization of clocks. Small, good clocks are useful, for instance, in the synchronization of communications networks and for improved military applications of global positioning systems [6, 7]. Rubidium standards, particularly those based on the phenomenon of coherent population trapping (CPT), are among the most promising candidates for miniaturization. This thesis presents two sets of experi-

ments that have implications for the development of such clocks.

First, we performed a series of tests characterizing and locking a vertical cavity surface emitting laser (VCSEL). In any passive timekeeping device, some external perturbation must be applied to the atoms for them to produce stable oscillations, which may then be used as a clock reference. Most designs use a laser for this. VCSELs are valuable in the construction of clocks because of their compact size. Also, more traditional edge-emitting diode lasers are subject to mode jumps at certain temperatures and currents. Occasionally these jumps occur directly at the frequency of interest, rendering the laser useless. VCSELs do not suffer from these problems [8]. The modulation bandwidth for a VCSEL is also typically large (on the order of multiple GHz). Thus, one may obtain phase-modulated sidebands at large modulation frequencies, and thereby generate a CPT resonance, with relative ease.

We successfully locked a VCSEL lent from Kernco to a variety of single photon resonances in rubidium vapor; applied high frequency modulation and tuned it to create a coherent population trapping CPT resonance; and characterized a number of laser attributes such as line width and maximal sweep speed. We also measured relative intensity noise increase as the laser was tuned to resonance and compared measurements of sideband amplitude depending on whether a Fabry-Perot cavity or a beat note signal was used as the detection mechanism.

Second, we explored the characteristics of the recently discovered  $N$ -resonance in  $^{87}\text{Rb}$  [9], which may prove to match or exceed the utility of coherent population trapping (CPT) as a reference in small-scale clocks. An earlier study showed that the  $N$ -resonance may have smaller light shifts and better contrast than a CPT resonance at buffer gas pressures of 25 and 40 Torr [10]. We tested a cell with 100 Torr of buffer gas. While light shifts and line widths were somewhat worse in such

a cell for the  $m_F = 0$  resonance, we found the contrast to remain strong, showing good promise for use in small clocks. Furthermore, the  $m_F = 1$  resonance does not appear to suffer from the same kinds of effects that  $m_F = 0$  does, suggesting that the  $N$ -resonance may be useful for magnetometry [11, 12].

The thesis is divided into five chapters. Chapter 2 gives theoretical background. Chapters 3 and 4 respectively relate the methods and results of the two tests described above. Chapter 5 suggests promising future studies.



# Chapter 2

## Theory

We outline in this chapter a few of the underpinning principles governing CPT and  $N$ -resonance phenomena. Both hinge on quantum interference effects, using multiple laser fields to couple atomic hyperfine structures.

### 2.1 Atom-light interaction

Derivations in both this and the next section were drawn primarily from reference [13], to which we refer the reader for a more detailed analysis. We give below a number of general relations between polarization, density matrix elements, and electric susceptibility.

#### Atomic polarization

When an electromagnetic wave passes through a vapor cell, it interacts primarily by inducing an electric polarization  $\mathcal{P}$  in the atoms, which in turn creates an electric field that couples back. The nature of this interaction is described by Maxwell's

equations in a medium,

$$\nabla \cdot \mathbf{D} = 0 \quad \nabla \times \mathbf{E} = -\frac{\partial \mathbf{B}}{\partial t} \quad (2.1)$$

$$\nabla \cdot \mathbf{B} = 0 \quad \nabla \times \mathbf{H} = \mathbf{J} + \frac{\partial \mathbf{D}}{\partial t} \quad (2.2)$$

where

$$\mathbf{D} = \epsilon_0 \mathbf{E} + \mathbf{P}, \quad \mathbf{B} = \mu_0 \mathbf{H}, \quad \mathbf{J} = \sigma \mathbf{E}. \quad (2.3)$$

Manipulation and considering only the  $z$  component of the field will lead to

$$-\frac{\partial^2 E}{\partial z^2} + \mu_0 \sigma \frac{\partial E}{\partial t} + \frac{1}{c^2} \frac{\partial^2 E}{\partial t^2} = -\mu_0 \frac{\partial^2 P}{\partial t^2}. \quad (2.4)$$

If  $E$  is approximately a sinusoidal function (with a quickly oscillating component and a slowly varying complex coefficient and phase), then  $P$  must also be approximately sinusoidal:

$$P(z, t) = \frac{1}{2} \mathcal{P}(z, t) e^{-i[\omega t - kz + \phi(z, t)]} + c.c. \quad (2.5)$$

For a two-level atom,  $P$  is also related to the density matrix element  $\rho_{ab}$  as

$$P(z, t) = \wp [\rho_{ab}(z, t) + c.c.] \quad (2.6)$$

where  $\wp$  is the dipole matrix element. Thus, we may derive the following equation for the complex polarization  $\mathcal{P}$ :

$$\mathcal{P}(z, t) = 2\wp \rho_{ab} e^{i[\omega t - kz + \phi(z, t)]}. \quad (2.7)$$

## Complex susceptibility

In a dilute gas we can define complex susceptibility  $\chi$  to be the relationship between complex polarization and electric field amplitude:

$$\mathcal{P} = \epsilon_0 \chi \mathcal{E}. \quad (2.8)$$

This value is fundamental to the description of an atomic interaction with an EM wave. For simplification purposes, we take  $\mathcal{E}$  to be real. We may then define the real and imaginary susceptibilities  $\chi = \chi' + i\chi''$  such that  $\chi'$  relates  $\mathcal{E}$  to the real part of  $\mathcal{P}$  and  $\chi''$  relates  $\mathcal{E}$  to the imaginary part of  $\mathcal{P}$ .

From equation (2.4), the following relationships may be derived:

$$\frac{\partial \mathcal{E}}{\partial z} + \frac{1}{c} \frac{\partial \mathcal{E}}{\partial t} = -\frac{\sigma}{2\epsilon_0 c} \mathcal{E} - \frac{1}{2\epsilon_0} k \text{Im} \mathcal{P} \quad (2.9)$$

$$\frac{\partial \phi}{\partial z} + \frac{1}{c} \frac{\partial \phi}{\partial t} = k - \frac{\omega}{c} - \frac{1}{2\epsilon_0} k \mathcal{E}^{-1} \text{Re} \mathcal{P}. \quad (2.10)$$

Thus, the real and imaginary parts of the complex polarization are directly related to the dispersion and absorption of light through the medium. If we take the case of a continuous wave ( $\mathcal{E}$  independent of time), in a medium with conductivity  $\sigma = 0$ , and index of refraction close to 1, the equations simplify to

$$\frac{\partial \mathcal{E}}{\partial z} = -\frac{1}{2\epsilon_0} k \text{Im} \mathcal{P}, \quad \frac{\partial \phi}{\partial z} = k - \frac{\omega}{c} - \frac{1}{2\epsilon_0} k \mathcal{E}^{-1} \text{Re} \mathcal{P}. \quad (2.11)$$

This is a good approximation in most cases. Substituting (2.8) into the left equation

above gives the following expression for absorption:

$$\mathcal{E} \approx \mathcal{E}_0 \exp\left(-\frac{1}{2}\chi''z\right). \quad (2.12)$$

The right equation in (2.11) shows that  $\phi(z, t)$  is linear with respect to  $z$ . However, the linear part of  $\phi$  should have already been factored into  $k$  (see equation (2.5)), so  $\phi$  is a constant with respect to  $z$  and its derivative is 0. Then we find an expression for the refractive index:

$$\frac{\omega}{c} = k \left(1 - \frac{1}{2}\chi'\right) = \frac{\omega}{c} n \left(1 - \frac{1}{2}\chi'\right) \quad (2.13)$$

$$n = \left(1 - \frac{1}{2}\chi'\right)^{-1} \approx 1 + \frac{1}{2}\chi'. \quad (2.14)$$

In the case of a two-level system the equation for susceptibility may be written as [14]

$$\chi(\Delta) = i\kappa \frac{\gamma/2 - i\Delta}{\gamma^2/4 + \Delta^2 + \frac{\wp^2|\mathcal{E}|^2}{\hbar^2}} \quad (2.15)$$

where  $\kappa \equiv N\wp^2/\epsilon_0\hbar$  is a proportionality constant,  $\gamma$  is a damping term due to spontaneous emission,  $\Delta = \omega_{atoms} - \omega_{probe}$  is the detuning from resonance,  $\wp$  is the dipole matrix element, and  $\mathcal{E}$  is the amplitude of the electric field. As a function of detuning, the corresponding absorption coefficient for this formula is Lorentzian, and the corresponding index of refraction is given by something roughly like the derivative of a Lorentzian. This effect both provides the lock-point feature for the single-photon lock, and the envelope which encloses both features described below.

## 2.2 Coherent population trapping/

### Electromagnetically induced transparency

Coherent population trapping (CPT) was discovered in 1976 [15] and observed in connection to electromagnetically induced transparency (EIT) in 1991 [16]. Throughout this thesis, the two terms will be used interchangeably. By one definition, CPT is the term used when referring to the interactions among atoms, and EIT is the term used when referring to the optics. We give below a model for understanding EIT as outlined in reference [13].

We take, as our model, a three state “ $\Lambda$ ” configuration with two ground states, coupled through two optical fields to the same excited state as depicted in figure 2.1. The drive field is strong, while the probe field is weak. The transition between the two ground states is forbidden.

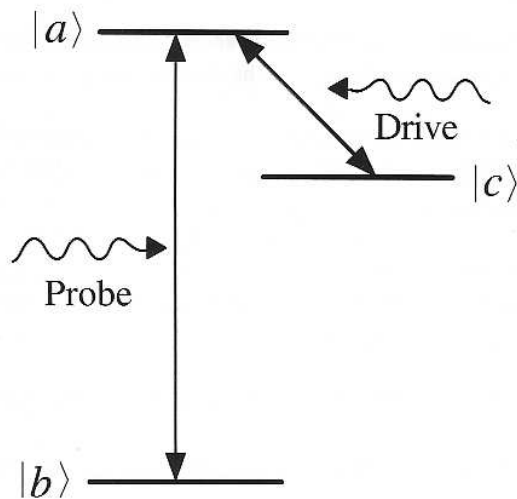


Figure 2.1: Level diagram for a simple manifestation of EIT [13]. The drive field is assumed to be much greater in magnitude than the probe. A transparency window also appears under equal probe and drive field intensities.

## Matrix elements

The Hamiltonian for such a system is given by

$$H = H_0 + H_1 \quad (2.16)$$

$$H_0 = \hbar\omega_a|a\rangle\langle a| + \hbar\omega_b|b\rangle\langle b| + \hbar\omega_c|c\rangle\langle c| \quad (2.17)$$

$$H_1 = -\frac{\hbar}{2}(\Omega_{R_1}e^{-i\phi_1}e^{-i\omega_1 t}|a\rangle\langle b| + \Omega_{R_2}e^{-i\phi_2}e^{-i\omega_1 t}|a\rangle\langle c|) + H.c. \quad (2.18)$$

which may be schematically written as

$$\mathbf{H} = \begin{pmatrix} \hbar\omega_a & -\frac{\hbar}{2}\Omega_{R_1}e^{-i\phi_1}e^{-i\omega_1 t} & -\frac{\hbar}{2}\Omega_{R_2}e^{-i\phi_2}e^{-i\omega_1 t} \\ -\frac{\hbar}{2}\Omega_{R_1}^*e^{i\phi_1}e^{i\omega_1 t} & \hbar\omega_b & 0 \\ -\frac{\hbar}{2}\Omega_{R_2}^*e^{i\phi_2}e^{i\omega_1 t} & 0 & \hbar\omega_c \end{pmatrix}.$$

The density matrix of the system is

$$\rho = \begin{pmatrix} \rho_{aa} & \rho_{ab} & \rho_{ac} \\ \rho_{ba} & \rho_{bb} & \rho_{bc} \\ \rho_{ca} & \rho_{cb} & \rho_{cc} \end{pmatrix}.$$

These two matrices are related through the Liouville equation:

$$\dot{\rho} = -\frac{i}{\hbar}[H, \rho]. \quad (2.19)$$

In our present weak-probe, strong-drive model, we may expect almost all of the atoms to be optically pumped into state  $|b\rangle$  to zeroth order. Assuming a weak probe also allows us to make the following substitution for the probe Rabi frequency:  $\Omega_{R_1} = \wp_{ab}\mathcal{E}/\hbar$ . Taking this into account and solving equation (2.19) above, one may

derive the following:

$$\rho_{ab}(t) = \frac{i\wp_{ab}\mathcal{E}e^{-i\omega t}(\gamma_3 + i\Delta)}{2\hbar[(\gamma_1 + i\Delta)(\gamma_3 + i\Delta) + \Omega_{R_2}^2/4]}. \quad (2.20)$$

Here, decay effects have also been taken into account by adding in the constants  $\gamma_1$  and  $\gamma_3$ . Detuning  $\Delta$  is defined  $\Delta = \omega_{ab} - \omega_1$ .

### Susceptibility

To obtain expressions for susceptibility of the probe field, we substitute equation (2.20) into equation (2.7) for  $\mathcal{P}$ , and substitute this into equation (2.8). We obtain the following:

$$\chi' = \frac{N_a|\wp_{ab}|^2\Delta}{\epsilon_0\hbar Z}[\gamma_3(\gamma_1 + \gamma_3) + (\Delta^2 - \gamma_1\gamma_3 - \Omega_\mu^2/4)] \quad (2.21)$$

$$\chi'' = \frac{N_a|\wp_{ab}|^2}{\epsilon_0\hbar Z}[\Delta^2(\gamma_1 + \gamma_3) - \gamma_3(\Delta^2 - \gamma_1\gamma_3 - \Omega_\mu^2/4)], \quad (2.22)$$

with atom number density  $N_a$  and

$$Z = (\Delta^2 - \gamma_1\gamma_3 - \Omega_\mu^2/4)^2 + \Delta^2(\gamma_1 + \gamma_3)^2. \quad (2.23)$$

Real and imaginary complex susceptibility are depicted pictorially in figure 2.2. The steep decline in  $\chi''$  reflects a sharp change in index of refraction for small detuning. This effect is responsible for the dramatically delayed group velocity effects also associated with EIT. We should note again that this derivation follows from the beginning assumption of a strong drive and weak probe. However, the qualitative phenomenon remains the same for equal intensity drive and probe.

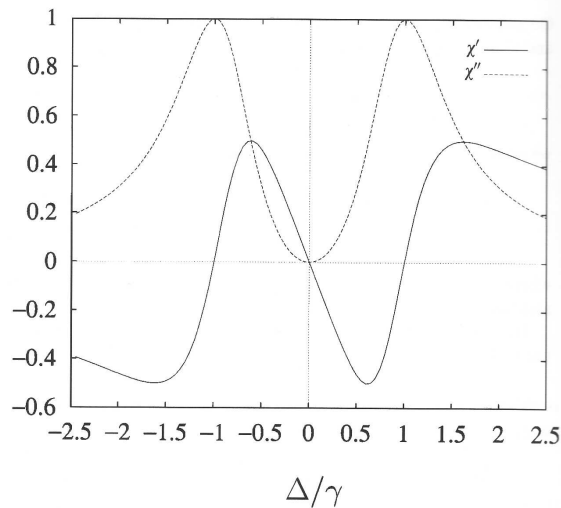


Figure 2.2: Plot of the real and imaginary components of the complex susceptibility for EIT [13]. At  $\Delta = 0$  the medium becomes perfectly transparent, but with a highly sloped refractive index.  $\Delta = \omega_{atoms} - \omega_{probe}$ , so in fact refractive index increases with probe field frequency in the transparent region.

### 2.3 $N$ -resonance

In 2002, A.S. Zibrov published a discovery of a new three-photon absorption resonance between coupled fields in rubidium vapor [9]. Further studies of the resonance have already shown it to be promising for small-scale clocks, with smaller light shifts and better contrast than a CPT resonance under comparable conditions [10]. Figure 2.3 shows the schematic layout of the energy levels and optical fields.

In reality, the effect can only truly be viewed as a three-photon coherent process, but qualitatively, one may think of this setup as a combination of a single-photon effect with the EIT effect. The single photon effect consists of the probe field connecting the upper ground state to the excited state. This provides an envelope absorption peak in probe transmission as a function of frequency.

The probe field also acts in conjunction with the drive field, coupling the two ground states and thereby optically pumping electrons into the upper ground state.

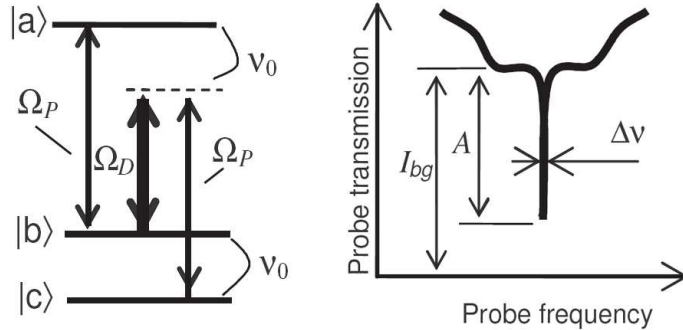


Figure 2.3: Level diagram for the  $N$ -resonance configuration. The corresponding transmission picture for the probe field as it is swept in relation to the drive is shown at right. It has a sharp absorption peak embedded within a larger, Doppler broadened peak.

This optical pumping effect only occurs when the drive and probe field are aligned so that their difference in frequency is exactly the frequency difference between the two ground states. This is a sub-Doppler effect, and therefore produces a much narrower resonance pattern on top of the Doppler-broadened peak.

The resonance is called an  $N$ -resonance because the three-photon path between energy levels schematically traces out an  $N$  (or an inverted  $N$ , in the above figure).

## 2.4 Resonances for clock use

In both the CPT and  $N$ -resonances, the absorption feature primarily depends on the frequency difference between the two fields. This value also corresponds to the ground state splitting of  $^{87}\text{Rb}$ : 6.835 GHz. If we then lock the detuning to the center of the resonance, we obtain a stable RF clock reference. In this manner, the nature of a CPT or  $N$ -resonance lies at the heart of the clock's functioning.

# Chapter 3

## VCSEL locking and characterization



Figure 3.1: A VCSEL from Kernco. Dimensions are about 1.5 cm by 1.5 cm by 0.5 cm.

A very important component of any passive atomic frequency standard is the probing field. In the case of a low power CPT or  $N$ -resonance clock, this likely takes the form of a vertical cavity surface emitting laser (VCSEL), for the reasons mentioned in Chapter 1. This chapter outlines the basic functioning and advantages

of VCSELs as compared to more standard edge emitting diode lasers, and discusses the results of a series of tests characterizing and locking one such laser, to be used eventually for clock tests like those described in Chapter 4. A test measuring the increase in relative intensity noise (RIN) when the VCSEL is tuned to resonance is of particular interest. Studies have shown that this noise increase has the potential to significantly degrade clock stability [17, 18].

## 3.1 VCSEL properties

To test VCSEL performance, the Walsworth Group borrowed a laser, pictured in figure 3.1, from Kernco. As may be seen, the lasing component itself is quite small. A small circuit card containing additional electronics for the laser extends a few centimeters below the VCSEL. Nominal optical power is  $216 \mu\text{W}$ <sup>1</sup>. See Appendix for more information.

### 3.1.1 Basic (unmodulated) properties

Before proceeding to lock and tune to resonance, we ran preliminary tests to characterize some of the laser's basic properties, including sensitivity to optical feedback, temperature change response rate, line width, and frequency stability.

#### Experimental setup

We configured the experimental setup as in the diagram in figure 3.2. All optics items are standard except for the isolator. Some form of isolation soon proved to be necessary as we discovered that much of the light sent toward the Fabry-Perot cavity, and some of the light sent to the Rb cell reflected back. The VCSEL was very

---

<sup>1</sup>Experimentally measured optical power was closer to  $150 \mu\text{W}$ .

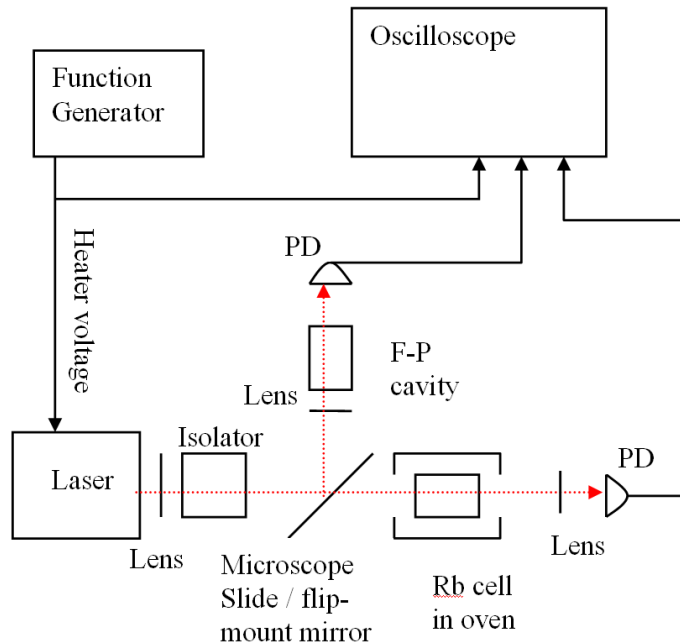


Figure 3.2: Block diagram of VCSEL setup for first tests. The laser and a collimating lens were enclosed within a small box in order to help minimize disturbance due to air currents. Then the beam was directed through a polarizing beam splitter and quarter-wave plate, which acted as an isolator. A small portion of the light was reflected by a glass slide and was directed through a focusing lens, a Fabry-Perot cavity, and finally to a photodetector on the other side. The rest of the light continued through an oven containing a vacuum cell of natural abundance  $^{87}\text{Rb}$  and  $^{85}\text{Rb}$  and was focused onto a second photodetector. Both photodetector signals were read from an oscilloscope on a nearby instrument rack.

sensitive to this, mode-hopping sporadically and exhibiting multi-mode behavior. At the same time, the shortest focal-length collimating lens available was 25 mm, resulting in a large beam diameter (about 1 cm). A beamsplitter and quarter-wave plate were able to accommodate both these requirements. A brief description of how these two elements work follows.

After having passing through the beam splitter, the laser light is linearly polarized. We may describe it by the Jones vector below<sup>2</sup>, ignoring the spatial component

<sup>2</sup>See <http://scienceworld.wolfram.com/physics/JonesMatrix.html> for more information on Jones vectors and matrices.

of the wave (as it does not concern us here), and normalizing to 1. It is convenient to choose a basis aligned with the angular orientation of the quarter-wave plate, with the fast axis as the  $x$ -axis.

$$\mathbf{J} \equiv \begin{pmatrix} E_x(t) \\ E_y(t) \end{pmatrix} = \begin{pmatrix} e^{-i\omega t} \cos \theta \\ e^{-i\omega t} \sin \theta \end{pmatrix} \quad (3.1)$$

A potentially interfering beam passes through the quarter-wave plate, reflects off of a mirror-like surface, and passes through the quarter-wave plate again. We may write the transformation as:

$$\begin{pmatrix} 1 & 0 \\ 0 & i \end{pmatrix} \begin{pmatrix} -1 & 0 \\ 0 & -1 \end{pmatrix} \begin{pmatrix} 1 & 0 \\ 0 & i \end{pmatrix} \begin{pmatrix} e^{-i\omega t} \cos \theta \\ e^{-i\omega t} \sin \theta \end{pmatrix} = \begin{pmatrix} -e^{-i\omega t} \cos \theta \\ e^{-i\omega t} \sin \theta \end{pmatrix} \quad (3.2)$$

This may be understood intuitively: passing through a quarter-wave plate twice is equivalent to passing through a half-wave plate once, thereby simply rotating the polarization. When we set  $\theta$  to 45 degrees, the polarization in the final reflected wave shifts by 90 degrees. Then the beam splitter will direct the reflected beam off to the side, instead of allowing it to interfere with the laser.

This setup was sufficient to eliminate multimode behavior and mode hopping almost completely. Still, it only works if polarization is preserved or inverted by all elements but the quarter-wave plate, so a fraction of reflected light may continue to feed back into the laser. As laser frequency was changed, we sometimes observed the transmission intensity from the Fabry-Perot cavity rise and fall at regular frequency intervals. This was a likely indication of feedback, as the effect was stronger when the Fabry-Perot cavity was better aligned.

## Unmodulated frequency stability

With the Fabry-Perot cavity in the setup as above, it was worthwhile to test how much the VCSEL drifts with no locking employed. Holding the VCSEL heater at a fixed voltage, we swept the length of the Fabry-Perot cavity over its full free spectral range (about 3 GHz), and examined the resulting transmission signal on the photodetector. Sophisticated analyses of the change in laser frequency as measured via this process over time would be possible, but a few minutes of watching soon revealed that the laser drifts more than 500 MHz over the course of a minute or so. Thus, it is clear that locking is necessary for the laser to be used as a practical tool.

## Temperature sweep characteristics

A simplified schematic of the Kernco VCSEL circuit is displayed in figure 3.3. We

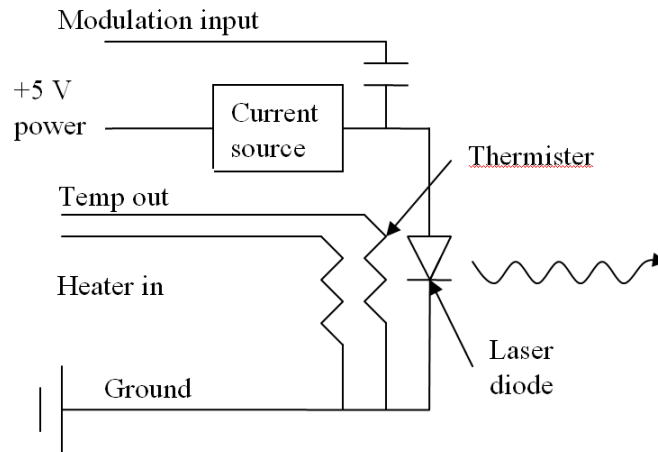


Figure 3.3: Qualitative schematic of the VCSEL circuit components. Laser frequency may be adjusted by changing temperature, or by applying an AC current modulation.

may manipulate laser frequency in one of two ways. One of these, the modulation

of laser current, is optimized for high frequency modulation (3.417 MHz). Capacitive coupling therefore blocks all DC and near-DC signals, and it is not possible to sweep the frequency, or make the fine frequency adjustments required for laser locking via this method. The alternative is to manipulate frequency by adjusting the temperature. This is limited by the fact that the frequency must be sufficiently low, or else the laser will not respond. Therefore we needed to determine how slowly the temperature should be changed for a linear response. We connected the heater input to a function generator, adjusted the function generator offset until the laser was close to rubidium resonance, and applied a small triangle wave sweep. If the sweep amplitude and frequency are low enough, we would hope to see a triangle sweep in laser frequency as well.

To search for a suitable frequency regime to run sweeps, we ran the following test, as outlined in figure 3.4. We adjusted the offset of the function generator so

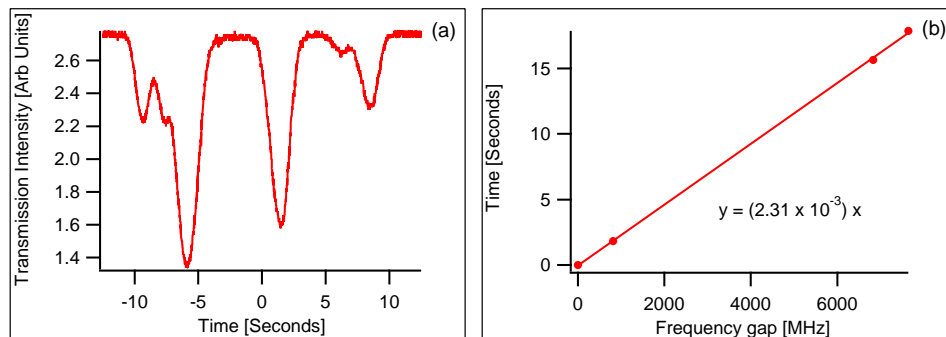


Figure 3.4: Example data for frequency sweep test. (a) shows the Rb cell absorption spectrum when the VCSEL was set to a triangle wave sweep, at 0.04 V and 0.01 Hz. Laser frequency increases from left to right. The optical depth here is about 20 percent for  $^{87}\text{Rb}$  peaks and roughly 40-50 percent for  $^{85}\text{Rb}$  peaks. (b) shows the corresponding plot used to calibrate time/frequency relationship, with differences between  $^{87}\text{Rb}$  peaks known to be 812, 6835, and 7647 MHz. The slope of the line in (b) indicates that 1 second along the  $x$  axis of (a) corresponds to about 433 MHz.

that the laser was tuned to the rubidium D1 resonance (794.76 nm). With the

VCSEL we were using, this meant heating the laser to about 75 degrees C, or to the point where the thermistor resistance had reduced from 100 k $\Omega$  down to 12.9 k $\Omega$ .<sup>3</sup> We found that 3.10 Volts was generally close to the appropriate offset voltage. On top of the offset we applied a small triangle wave at fixed amplitude (either 0.07 V or 0.04 V). Then, we saved pictures of the rubidium resonance at various sweep frequency settings.

The distances between the absorption peaks of  $^{87}\text{Rb}$  are well-known values (see figure 3.5), and for a given test run, we may measure the distance between all these

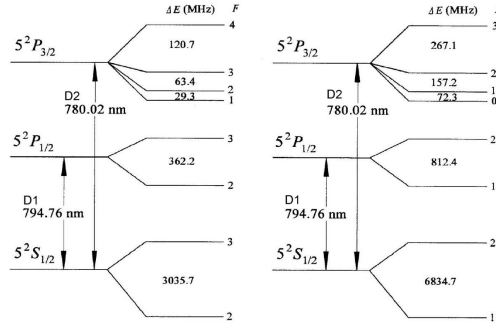


Figure 3.5: Level diagram for  $^{85}\text{Rb}$  and  $^{87}\text{Rb}$ . Most measurements of interest in this thesis probe the 6.8 GHz hyperfine splitting between the ground states of  $^{87}\text{Rb}$ , connecting them optically via the D1 transition to a  $5^2P_{1/2}$  excited state.

peaks in time. We may then calibrate the rate at which the laser frequency changes as it crosses the resonance. Such a calibration is shown in figure 3.4b.

Furthermore, if the sweep is sufficiently slow, the rate of frequency change will be a constant, and we may extrapolate an estimation of the full sweep range of the VCSEL. If the voltage sweep changes too quickly, then the rate of frequency change will become distorted, and our estimation of the full sweep range of the VCSEL will

<sup>3</sup>More detailed calibration information between the thermistor output and laser temperature is available in the appendix.

be inaccurate. More importantly for diagnostic purposes, this inaccurate estimation will also be frequency dependent. Thus, we may get some indication of how nicely the laser is being swept by calculating “full sweep ranges” for a series of sweep frequencies at a given sweep amplitude, and examining them to see when they level out.

Figure 3.6 shows the test as performed in two regimes. The test in 3.6a has an input amplitude of 0.07 V, offset roughly 3.10 V, and frequency 0.05-0.5 Hz. The sweep rate was too fast for nearly all of these frequencies, as demonstrated by the fact that the calculated range consistently drops in the figure, first quickly between 0.05 and 0.1 Hz, and then more slowly between 0.1 and 0.5 Hz. Figure 3.6b shows the test with input amplitude 0.04 V and frequency 0.01-0.05 Hz. Here, the sweep has leveled out, and so it appears that 0.01-0.04 Hz at amplitude 0.04 V is an acceptably gentle sweep rate. The range, which maxes out at 23 GHz, also allows us to infer that laser frequency changes with respect to applied voltage at a rate of roughly 290 MHz/mV near resonance.

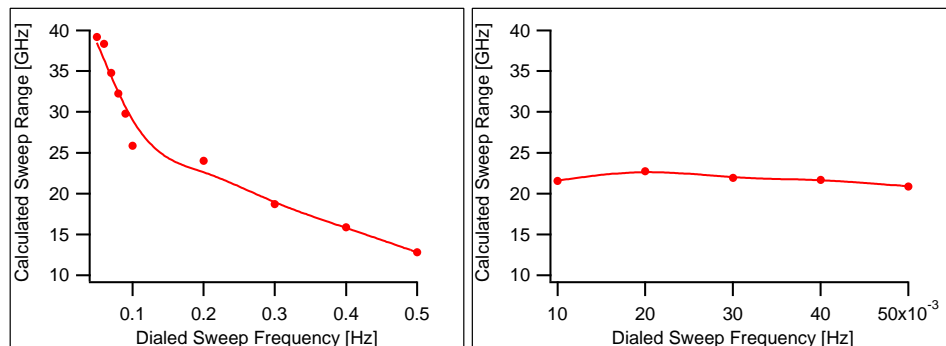


Figure 3.6: VCSEL sweep tests. (a) shows calculated ranges for an input amplitude of 0.07 V, between 0.05 and 0.5 Hz. (b) shows calculated ranges for an input amplitude of 0.04 V, between 0.01 and 0.05 Hz.

The linearity of the frequency sweep in figure 3.6b can be verified through simul-

taneous examination of the signal emerging from the Fabry-Perot cavity. If the laser is increasing frequency at a constant rate, then if we hold the cavity length fixed, we may expect to see resonances that are evenly spaced in time, corresponding to the laser resonating in the cavity as it passes through successive integer multiples of the free spectral range. An example sweep showing both the rubidium resonance and Fabry-Perot cavity resonances is shown in figure 3.7, and the corresponding test of sweep linearity for the 0.01 and 0.05 Hz sweeps is displayed in figure 3.8. Both sweeps are quite linear.

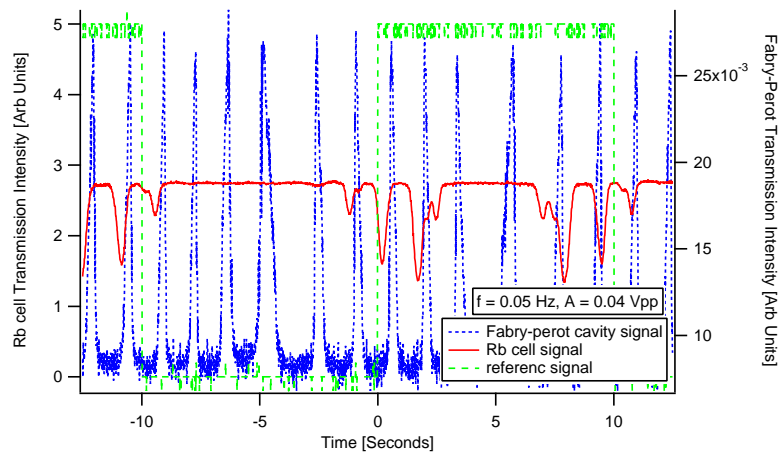


Figure 3.7: Another sweep of the rubidium resonance (red solid line), this time with the Fabry-Perot Cavity monitored at the same time (blue hashes). The square wave of green dashes indicates the sweep reference. The sweep rate of the triangle wave is about 2.08 GHz/sec. Sweep frequency is 0.05 Hz.

### Laser line width and verification of Fabry-Perot FSR

The preceding test also allowed us to measure laser line width and to make a brief check of the free spectral range of the Fabry-Perot cavity.

Using a Fabry Perot resonance picture like the one in figure 3.7, we measured the time between resonance peaks to be  $0.749 \pm 0.008$  seconds. We then used the

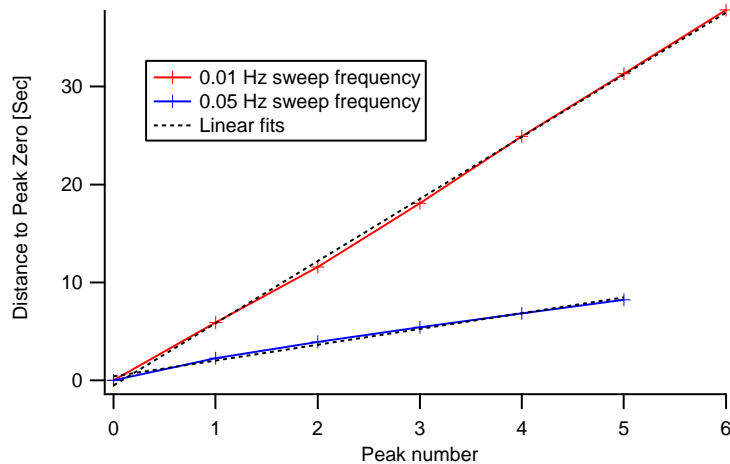


Figure 3.8: Fabry-Perot resonances (see figure 3.7) plotted against time for 0.04 V at 0.01 and 0.05 Hz. Peak zero was selected as the peak furthest to the left in a given sweep (at -4.86 seconds in figure 3.7 because the sweep begins at -5 seconds), peak one was selected as the peak immediately to the right of peak zero, and so on. Both plots are linear, verifying a linear sweep at these frequencies. Adjacent peaks are always separated by the free spectral range in frequency, about 3.06 GHz.

absorption peaks to calibrate a time/frequency relationship of  $2.45 \times 10^{-4} \pm 6 \times 10^{-6}$  seconds/MHz. Dividing these two values, we calculated the FSR of the Fabry-Perot cavity to be  $3.06 \pm 0.08$  GHz when no voltage is applied to the piezo element.

Similarly, if we assume that the Fabry-Perot cavity's finesse is negligible compared to the laser line width, then the width of the cavity resonance peaks is equal to the laser line width. Measuring full-width, half-max values of these peaks, we found a line width of  $0.114 \pm 0.006$  seconds, or  $460 \pm 25$  MHz. The width calculation may be somewhat inaccurate, however, as Fabry-Perot resonances were systematically asymmetrical. Perhaps the laser was sweeping too fast for detection mechanisms to respond.

Error in these measurements was calculated by assuming Gaussian variation of noise in the figure, and then accounting for error propagation using the standard

formula:

$$\sigma_z = \sqrt{\left(\frac{\partial z}{\partial x_1}\right)^2 \sigma_{x_1}^2 + \left(\frac{\partial z}{\partial x_2}\right)^2 \sigma_{x_2}^2 + \dots} \quad (3.3)$$

### 3.1.2 Modulated properties

Both the CPT and  $N$ -resonance effects discussed in chapter 2 require two coherent coupling beams of different frequency. This may be accomplished by using two distinct phase-locked lasers. However, such a configuration is both expensive and bulky, and so usually other means are sought out. The most widely employed method is to use a single laser and, either through the use of an electro-optic modulator (EOM) or through direct current modulation, modulate the laser phase at the desired splitting between coherent fields, thereby creating sidebands. A VCSEL is well-suited to this type of manipulation, with a modulation bandwidth on the order of multiple GHz. In the subsection below we discuss the theory of phase modulation, outline some of the necessary measures required to make large sidebands a reality, and display some data characterizing the amplitude that the sidebands attained.

#### Theory

Phase modulation may be written mathematically as

$$E(t) = E_0 \cos(\omega_c t) \rightarrow E = E_0 \cos(\omega_c t + M \sin \omega_M t). \quad (3.4)$$

Here,  $\omega_c$  is the carrier frequency,  $E_0$  is the amplitude,  $\omega_M$  is the modulation frequency, and  $M$  is the modulation amplitude, hereafter known as the modulation index. Because instantaneous frequency is the derivative of the phase, this also

corresponds to frequency modulation:

$$\omega \equiv \frac{\partial \phi}{\partial t} = \omega_c + M\omega_M \cos \omega_M t. \quad (3.5)$$

Equation (3.4) above may be re-expressed as a sum of Bessel functions in the following manner<sup>4</sup>:

$$E(t) = \frac{E_0}{2} \sum_{n=-\infty}^{\infty} J_n(M) e^{i(\omega + n\omega_M)t} + c.c. \quad (3.6)$$

Taking the Fourier transformation of this reveals a series of monochromatic EM fields which are spaced over integer multiples of the modulation frequency, and which have amplitude equal to their respective Bessel function coefficients (see figure 3.9).

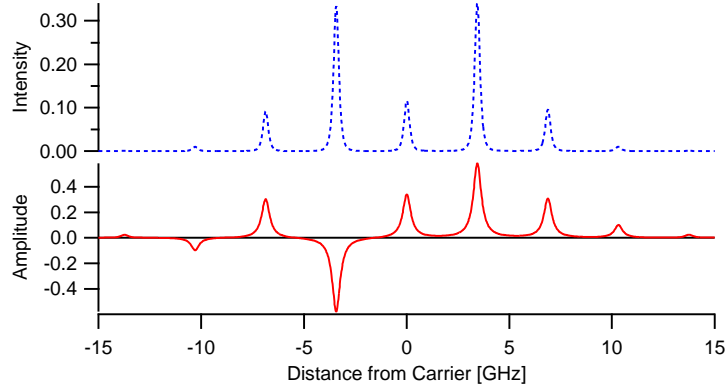


Figure 3.9: Theoretical sidebands in frequency space for modulation index 1.8, 300 MHz intensity line width, and 3.417 GHz modulation frequency. The solid red plot on the bottom shows amplitude; the blue hashes plotted above it are amplitude squared, or intensity.

Thus, by phase-modulating with varying degrees of frequency and modulation index, we may create sidebands at a wide variety of amplitudes and frequency off-

<sup>4</sup>See <http://mathworld.wolfram.com/BesselFunctionoftheFirstKind.html>, eq. 64., or reference [19].

sets. Note that in order for the sidebands to be of any appreciable amplitude, the modulation index must be large, which is possible with a VCSEL.

## Experimental setup

A block diagram of the experimental setup for applying high frequency modulation to the laser is displayed in figure 3.10. Configuration is as in figure 3.2 except for a new cable attached to the high frequency input on the VCSEL. We applied a 3.417 GHz signal through this cable.

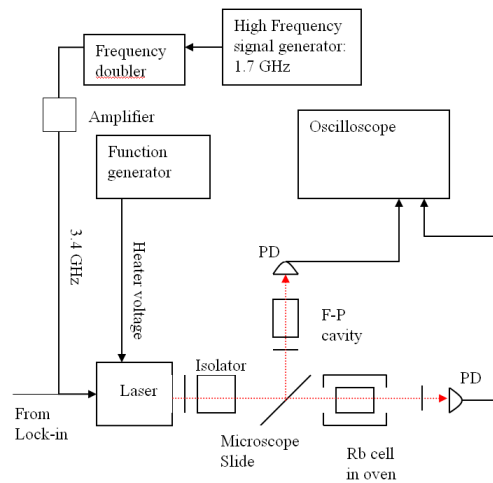


Figure 3.10: Block diagram of VCSEL setup with high frequency modulation. Setup remains the same as in figure 3.2, aside for the components on the upper left side.

We needed the frequency doubler because the high frequency signal generator did not have a 3.4 GHz range. The doubler suffered a loss of about 10 dB in the process (it was not technically rated in this frequency range), but the installation of an amplifier made up for this. The VCSEL’s documentation (Appendix) says that 3.5 dBm are required to produce a modulation index of 1.8. This is well within the output range of the combined HF signal generator, frequency doubler, and amplifier

setup. However, ensuring that as much as 3.5 dBm also made it into the VCSEL was a considerable challenge due to reflections. We installed a directional coupler (which can give one-way readings of both the signal coming from the signal generator and the signal returning from the VCSEL) between the amplifier and laser to diagnose these reflections.

The design was further complicated by a necessary tee-connector linking a BNC cable that would be used later to feed in a 10 kHz reference signal for locking. At one point, we tried using an SMA bias-tee to prevent loss through this connection. This failed to work because of reflections. As we turned up the input power on the high frequency generator, the sidebands got larger, but they also became severely asymmetrical, and it became impossible to tell the sidebands from the carrier. Putting a standard SMA tee in the same position seemed to suppress reflections, possibly by creating a node at that point in the line, so we used this configuration.

### **Maximizing modulation index**

A characteristic picture of the sidebands eventually obtained is shown in figure 3.11. At this modulation index, several higher order sidebands beyond the first-order sideband become visible, and even comparable to the carrier, which diminishes greatly in amplitude as modulation index increases. In general these will create effects contributing to light shifts in the atoms' energy levels. However, in theory when the modulation index is 2.4, second and third-order sideband effects, along with that of the carrier, will all cancel each other out, decreasing the overall light shift to zero [8].

The Fabry-Perot cavity may be used to give an approximation of the modulation index. Using a fitting procedure, we inferred  $M \approx 1.8$  (see figure 3.12).

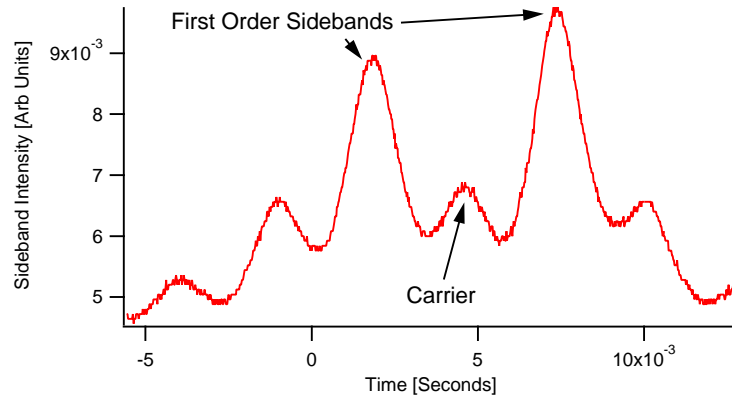


Figure 3.11: An image from the Fabry-Perot cavity of sidebands modulated at high frequency. Modulation index here is about 1.8. 1 ms corresponds to roughly 130 MHz. Sidebands overlap each other here because the free spectral range compresses the picture, making a distance of 3.417 GHz look like 360 MHz. In this figure, laser frequency decreases from left to right.

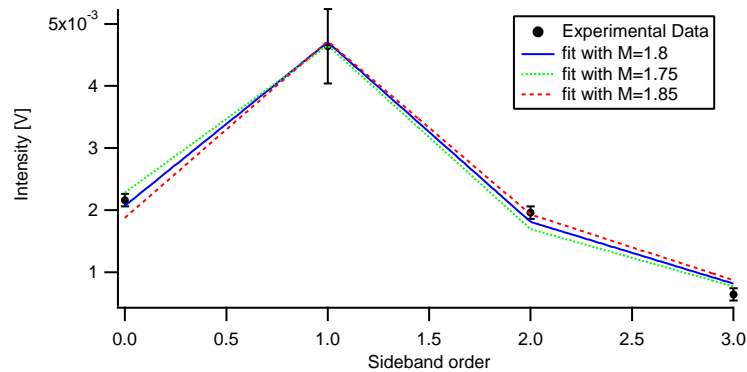


Figure 3.12: Sideband intensities, as measured in figure 3.11, are plotted and varying fits are used to estimate  $M$ . The primary source of error in the first order bands is due to amplitude modulation.

## 3.2 Laser locking

As mentioned in section 3.1.1, it soon became apparent that some form of laser stabilization configuration would be necessary. Thus, it was important to implement and test a locking configuration with the Kernco VCSEL. In a rubidium CPT or  $N$ -resonance clock, two separate locks must be implemented: one to lock the 795

nm (377 THz) single-photon transition, and one to lock the 6.835 GHz two-photon transition. Below we concern ourselves with locking only the one-photon transition, with and without high frequency modulation.

### 3.2.1 Experimental setup

A block diagram of the experimental setup used for locking is displayed in figure 3.13. The two most important new components in this diagram are the lock-in

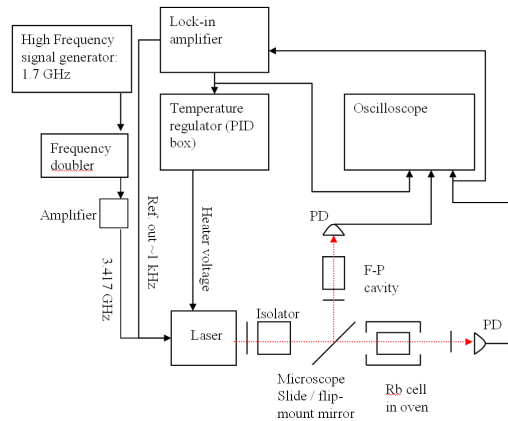


Figure 3.13: Block diagram of VCSEL with single-photon transition locking. Almost all of the optical equipment used is the same here as it was in the original tests of basic laser characteristics. The only difference in this part of the setup is that for many of the experiments, the vacuum cell and heater were replaced by a shielded cell of only  $^{87}\text{Rb}$  and 3 Torr of Ne buffer gas. Both cells are 7.5 cm long and 2.5 cm in diameter. Using a cell without  $^{85}\text{Rb}$  made it easier to lock to a transition where EIT could be seen, and adding in the magnetic shields made EIT observation possible later on.

amplifier and PID box. Their functions in this setup are described in detail below.

#### Lock-in amplifier

Locking a variable is generally achieved by monitoring some signal which, to first order approximation, is proportional to the difference between the variable of interest and the set point. Thus, if the variable is above the set point, the monitoring signal

will be (for example) positive, and the control system can be set to decrease the variable. If the variable is below the lock point, then the monitoring signal will be negative, and the control system will increase the variable.

In the case of locking to a transition line of rubidium, however, we are faced with a problem. It is sensible to try to use the transmitted intensity of the probe as our monitoring signal (because a photodetector may detect this easily), and it is desirable to lock to the center of the resonance at the bottom of the transmission peak. However, because this is a minimum, we don't know whether the laser is drifting above or below the set point if we see transmission increase.

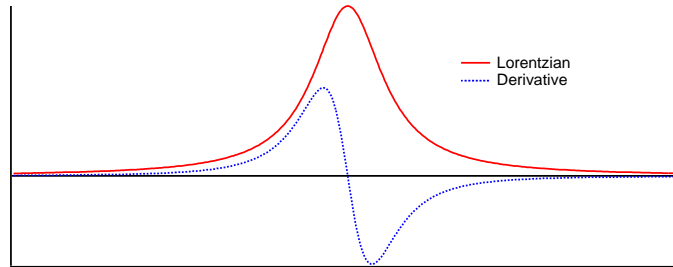


Figure 3.14: An example Lorentzian absorption line shape (solid red line) and first derivative (dotted blue line). Where the absorption is maximal (transmission minimal), the first derivative has a distinct zero crossing.

The lock-in amplifier provides a convenient solution to this problem. Instead of simply sending a monochromatic beam through the rubidium cell, we modulate it with a small modulation index and frequency, specifically

$$E = E_0 \cos(\omega_c t + m \sin \omega_m t), \quad m \ll 1, \omega_m \ll \delta \quad (3.7)$$

where  $\omega_c$  is the carrier frequency,  $m$  is the locking modulation index,  $\omega_m$  is the locking modulation frequency, and  $\delta$  is the characteristic width of the resonance,

typically 500 MHz full-width half-max for a Doppler-broadened rubidium resonance at room temperature. The instantaneous frequency is then

$$\omega \equiv \frac{\partial\phi}{\partial t} = \omega_c + m\omega_m \sin \omega_m t. \quad (3.8)$$

Thus, in frequency space, the laser oscillates back and forth about center frequency  $\omega_c$  with amplitude  $m\omega_m$  and frequency  $\omega_m$ .

Because  $m\omega_m$  is small, we may approximate the change in transmission intensity  $I$  corresponding to the change in frequency  $\omega$  by the differential

$$dI = \left( \frac{\partial I}{\partial \omega} \right) d\omega. \quad (3.9)$$

We use the lock-in amplifier to pick up variations in the component of the transmission signal oscillating at frequency  $\omega_m$ . As equation (3.8) shows,  $d\omega$  is of this form, and so the lock-in amplifier picks out the derivative of the transmitted intensity with respect to frequency. In contrast to the raw transmission signal, this provides a good lock point (see figure 3.14).

## **PID box**

In order to maintain an effective lock, we need a control mechanism to respond to the feedback signal produced by the lock-in amplifier. This is the function of the PID (proportional, integral, and differential) controller. Such controllers are described in reference [20].

In short, the PID box corrects a constant voltage supplied by a quiescent heater via three mechanisms. First, it adjusts the output signal by an amount proportional to input. Thus it responds more strongly to correct a signal for which the monitor

value is far from the set point, and responds more weakly as the error decreases. Second, it adjusts its output signal by a value proportional to the integral of the error signal. This accounts for longer-term variation in the constant power required to maintain the lock. Finally, the controller responds with a correction proportional to the derivative of the feedback signal. This accounts for situations when the set point varies rapidly. In our experiment, the set point is a rubidium transition line, which is unvarying, so we employed only the P and I components of the temperature controller.

### 3.2.2 Locking procedures

#### Open-loop response

As mentioned above, the lock-in amplifier is capable of detecting a signal modulated at  $\omega_m$ . If the lock-in is not directly in phase with the laser intensity signal, then it won't detect as strong a response signal as it could. If it is more than 90 degrees out of phase, the output of the lock-in is an inverted signal, and the locking setup will actually push the laser frequency away from the set point.

To optimize the phase, the laser was tuned manually on resonance. Then the lock-in phase was adjusted so that the output on the  $x$  channel was maximized. (With this particular lock-in, there was an "auto phase" button which did this electronically.) It remained to be seen that this setting was in phase with the signal, and not shifted 180 degrees.

To check this, we ran an open-loop response. This procedure consists of breaking the lock-loop depicted in figure 3.13 between the output of the lock-in amplifier, and the input of the PID box. Instead, a function generator was connected to the PID input and set to sweep across the resonance (with an amplitude of about 0.04 V

and frequency about 0.01 Hz). PID gain was set to 1 and both the integrator and differentiator were turned off. An example open loop response is shown in figure 3.15.

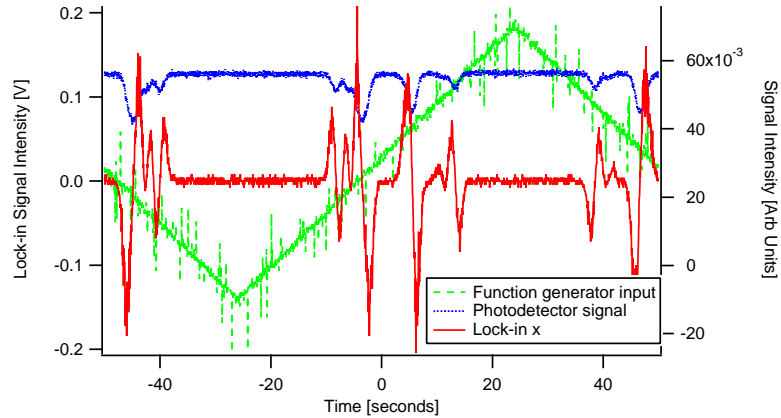


Figure 3.15: An open-loop response for natural abundance rubidium. The sweep rate is about 360 MHz/second. The solid red line is the lock-in response, the dotted blue line is transmission intensity, and the dashed green line is a frequency reference. Note the noise in the reference signal. This is a possible indication of ground loops.

Using this configuration, we were able to observe the lock-in response as the laser frequency increased. As function generator voltage increased, we saw that laser frequency also increased. (The orientation of a natural abundance rubidium resonance may be identified by noting that on the low frequency side, the  $^{87}\text{Rb}$  peaks merge with the  $^{85}\text{Rb}$  peak, while on the high frequency side, they stand alone.) Ideally, the lock-in amplifier response would slope in the opposite direction to the voltage sweep in the immediate neighborhood of a resonance, so as to provide an appropriate corrective measure. This was found to be the case in the particular sweep shown when the lock-in phase was set to about 70 degrees. This phase calibration is not universal, and different optimal settings were found for different configurations of components.

Several open loop responses were also taken for the shielded cell of  $^{87}\text{Rb}$ , and

one is included in figure 3.16 for comparative purposes. It may be slightly more difficult to identify the orientation in this case, but the high frequency side of the resonance is the more asymmetrical of the two. Thus, this diagram shows a correct lock-in phase, at 120 degrees.

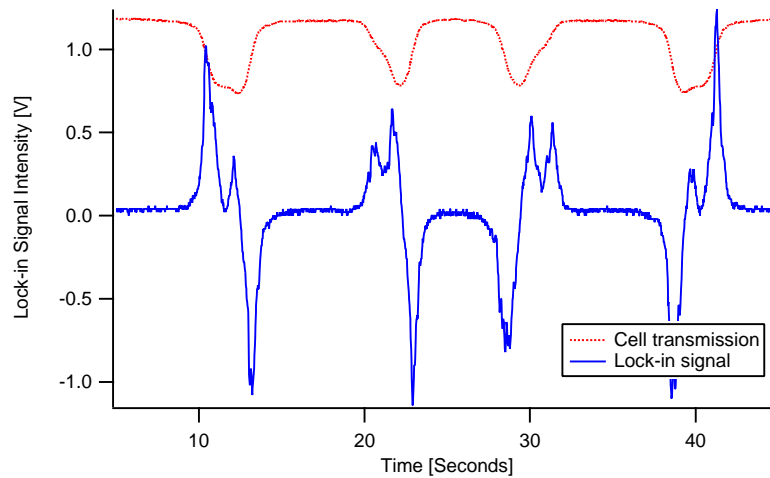


Figure 3.16: An open-loop response curve for an isotopically enriched cell. The sweep rate is about 700 MHz/second. Red dots correspond to transmission. The blue line corresponds to the lock-in response. The more asymmetrical of the two resonances is the high frequency side. A mirror image appears on the right hand side as the sweep reverses direction.

The characteristics of the open loop response were also useful as a diagnostic tool, letting us know which settings gave better signal to noise ratios in the lock-in output. As figure 3.15 shows, many of the initial settings produced open loop response curves that were fairly noisy. Noise in the sweep curve coming from the function generator seems to indicate ground loops.

### Setting and stabilizing the lock

As mentioned above, we employed only the proportional and integral components of the temperature controller. A specific expression for its output is given by:

$$V_{out}(t) = V_0 - G(V_{in}(t) - V_{offset}) - \frac{G}{T_1} \int_{t_0}^t [V_{in}(t') - V_{offset}] dt' + V_c. \quad (3.10)$$

Here,  $V_0$  is the quiescent heater voltage,  $V_{in}$  is the input voltage from the lock-in amplifier,  $V_{offset}$  is an offset voltage,  $G$  is gain,  $T_1$  is a proportionality constant of the integrator,  $t_0$  is the time the apparatus was turned on, and  $V_c$  is a correction term to account for charge on the integrating capacitor at the time the box was turned on. Everything except for  $V_c$  and  $V_{in}$  may be adjusted manually.

We found a fairly straightforward procedure for locking using this equation. With the loop open (making  $V_{in} = 0$ ), we turned on the integrator and applied a small offset, which caused the laser to gradually sweep across the resonance. When the laser passed over the resonant peak of interest, we closed the loop. If parameters were favorable, the laser locked immediately. When the lock-in amplifier provided an open-loop response ranging within  $\pm 500$  mV, we found that  $G$  set to 0.03, and  $T_1$  set to 1 second were usually good values. The temperature controller used also had an additional dial for a frequency cutoff ( $T_2$ ), which we set to 0.03. These settings are not optimized.

### 3.2.3 Locking with HF modulation

In order to see EIT it is necessary to lock the VCSEL while it is being modulated at high frequency, so that the sidebands will be present to couple the hyperfine rubidium transition. All of the procedures followed above remain the same, except

that the observed resonance pattern as the laser sweeps from low frequency to high frequency changes. Reexamining figure 3.16, note there are two distinct resonance peaks (with internal structure) as a monochromatic beam sweeps from low to high frequency. These are separated by 6.8 GHz. When the high frequency modulation is turned on, the laser splits into a series of sidebands at 3.4 GHz intervals, exactly half the distance between the resonance peaks (recall figure 3.9). Thus, as the laser sweeps from low to high frequency, the sidebands will pass over the resonance in synchronization and a string of resonance peaks, spaced evenly at 3.4 GHz intervals, will be observed at the photodetector output. In most cases, the modulation index will be adjusted so that the two first order sidebands dominate; in this case, the largest resonance peak will occur when the lower sideband passes over the lower resonance and the upper sideband passes over the higher resonance.

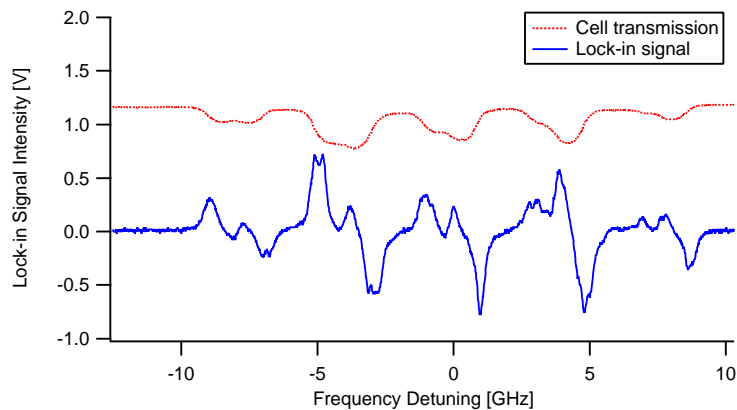


Figure 3.17: An open-loop response curve for high-frequency modulation. Red dots correspond to transmission. The blue line corresponds to the lock-in response. The resonance with the strongest EIT sits in the center, slightly smaller than the resonance on either side because a relatively small index of modulation was used. (The sidebands were roughly 1/6 of the carrier’s intensity.)

An example open loop response when the laser is modulated at high frequency is displayed in figure 3.17. There, the modulation index is small, so that the sideband

intensities were only about 1/6 the carrier, and the resonance peak where the first order sidebands pass over the rubidium resonance is slightly smaller than the peak on either side. We may discern the orientation of the resonance pattern by noting that in any given resonance peak, the larger sub-peak will be on the high frequency side.

### 3.2.4 Locking off resonance

Besides locking to the center of a resonance peak, we were also able to lock to points within a neighborhood of the peak, by adding or subtracting an offset to the lock-in output signal. This is illustrated in figure 3.18. When no offset is applied, the lock-in signal crosses zero at about 34 seconds on the x-axis. If a small negative offset is applied, then the zero crossing shifts down in frequency, however. If the negative offset is large enough, then it can even push the lock onto a different resonance. By this method, one may readily lock to the  $F = 1 \rightarrow F' = 1, F = 2 \rightarrow F' = 1$  transition on the left side of the center resonance, which would otherwise be difficult to access.

In the region about the set point where the open loop response is linear, we also calibrated the relationship between dialed offset, in volts, and shift in the set point, in hertz. This was done in two stages. First, a linear fit was performed about the set point, yielding the equation

$$V = \text{Const.} - (0.0791 \pm 7 \times 10^4)t \Rightarrow m_1 = -0.0791 \text{ V/s.} \quad (3.11)$$

This gave a relationship between offset voltage and time. Next, the resonance peaks in the transmission signal were used to calibrate a relationship between time and

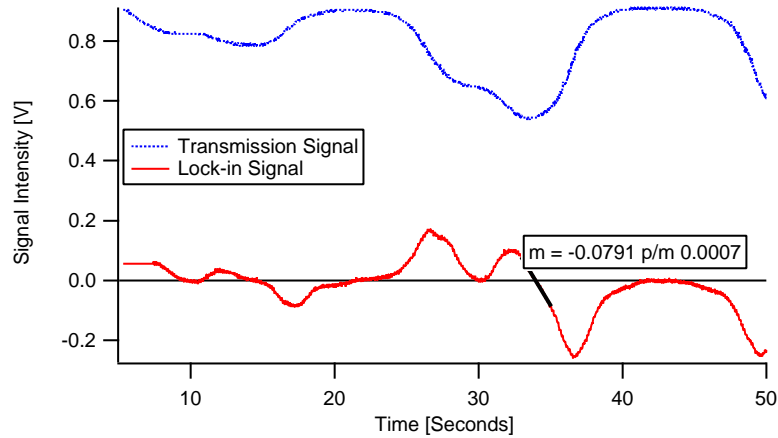


Figure 3.18: Open-loop response curve used to calibrate a relationship between lock-in offset voltage and time. The sweep rate is about 170 MHz/second. The function generator sweep for this figure was very gentle, in order to ensure that the lock-in output signal during the open loop response was truly representative of the lock-in output signal when the lock-loop is closed. (In prior cases, a faster sweep speed caused the lock-in amplifier to average over too much time, and the open-loop response lock-in output looked smaller than it actually was when the system was locked. This was not important for figuring out the phase.) With the lock-in time constant set to 100 ms, we swept the function generator feeding into the PID box at 0.01 Hz and 0.02 V. As in all other open-loop responses, PID gain was set to 1, and the integrator and differentiator were off.

frequency, yielding<sup>5</sup>

$$t = (0.0059 \pm 0.0001)\nu \Rightarrow m_2 = 0.0059 \text{ s/MHz}. \quad (3.12)$$

To calculate the relationship between volts and megahertz, we simply multiply  $m_1$  by  $m_2$ , yielding

$$m_1 m_2 = 0.47 \pm 0.01 \text{ mV/MHz}. \quad (3.13)$$

Error was calculated using equation 3.3. This estimation should be valid for all distances from the set point for which the lock-in response is linear, roughly  $\pm 170$  MHz or  $\pm 80$  mV. This result is not universal, as it depends on the sensitivity setting

---

<sup>5</sup>This is the same method as was used in section 3.1.1 to calculate laser linewidth and free spectral range.

of the lock-in amplifier, the cell temperature, and several other factors.

### 3.2.5 Ground loops

As the lock loop was being assembled, it quickly became apparent that ground loops would be a potentially serious problem. As mentioned before, in figure 3.15, the reference or the function generator sweep was considerably noisier than it should have been. When disconnected from the PID box, this extra noise went away. We therefore refrained from connecting unnecessary cables.

A particularly problematic section of the setup, possibly due to ground loops, existed at the photodetector. Four key components all merged here: the photodetector, a photodetector box, the lock-in amplifier input, and the oscilloscope. It was difficult at first to get lock-in response signals that were both free of noise and replicable. Initially, the lock-in time constant was set to  $300\ \mu\text{s}$ , and the lock-in frequency was set to 1 kHz. This worked, but response signals were noisy, as can be seen in figure 3.17. More problematic, the response signal looked significantly different on different passes, making calibration efforts difficult. Increasing the lock-in time constant to 100 ms did a lot to fix this problem. It was also very helpful to turn the modulation frequency up to 10 kHz. Increasing modulation frequency produced its own problems, however. Although the BNC connection between the photodetector and the cable running to the oscilloscope worked without problem for the 1 kHz signal, it had significant loss at 10 kHz. Thus, very little of the 10 kHz signal made it to the lock-in amplifier input. We fixed this problem by putting a  $1\ \text{M}\Omega$  resistor between the photodetector and the cable running to the oscilloscope. While it cut the signal at the oscilloscope in half (the oscilloscope input impedance was  $1\ \text{M}\Omega$ ), there was a good signal to noise ratio in the transmission.

## 3.3 EIT realization and characterization

### 3.3.1 Procedure

Once the first-order sidebands had been locked to their transitions connecting the  $^{87}\text{Rb}$  hyperfine splitting, it was possible to observe electromagnetically induced transparency (EIT) by sweeping the 3.4 GHz signal. The setup, precisely the same as that in figure 3.13 aside from the addition of a function generator used to drive the modulation of the HF signal generator, is shown in figure 3.19.

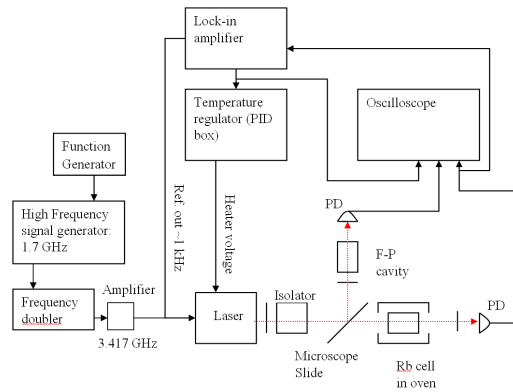


Figure 3.19: Block diagram of VCSEL with single-photon transition locked, and two-photon transition sweeping. This configuration allowed us to observe EIT.

The HF signal generator was set so that frequency modulation was on, with external DC modulation. Under external DC modulation one can supply any signal oscillating between DC and 150 kHz. In order for the range of frequency modulation on the HF signal generator to be correctly calibrated, the external source must be providing 1 Vpk into a  $600 \Omega$  input<sup>6</sup>. The internal resistance of the function generator was  $50 \Omega$ , so this meant that a dialed amplitude on the function generator of  $650/600$  V, or 1.08 V, was required. The function generator was set to a triangle

<sup>6</sup>See p. 1 b-52 in the manual for the Agilent 8648B, which was the signal generator we used.

wave. The HF signal generator was set to a center frequency of 1708.67065 MHz, and was set to modulate with a 25 kHz amplitude. Thus, the span of the HF function generator was 50 kHz. The frequency doubler doubled this sweep range, and it was doubled again because the modulation moved both sidebands by the same amount in opposite directions, so the total frequency span probed was 200 kHz.

It was necessary to have the magnetic shielding in place around the cell for any features to be seen. Otherwise the Zeeman splitting of the energy levels would have dispersed the sublevels over too large of a frequency range to be detectable.

### 3.3.2 EIT observation

Under these conditions, we saw EIT. An example resonance peak is depicted in figure 3.20. The laser fields here connect the  $F = 1$  and  $F = 2$  hyperfine ground states of  $^{87}\text{Rb}$  to the  $F' = 2$  excited state.

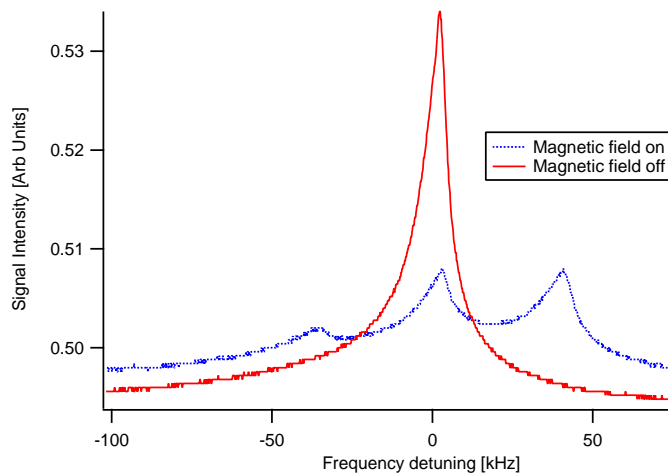


Figure 3.20: An EIT transmission peak. Contrast, defined as the feature height divided by baseline transmission, is maximally near 8 percent. Full-width half-max linewidth is about 11 kHz. The baseline optical depth is about 40 percent, as may be seen visually in figure 3.18. The blue dotted line reflects when a small uniform magnetic field has been applied, splitting the resonance into its three magnetic sublevels. Optical pumping into the end-states is apparent.

We confirmed that this was EIT by applying a small current through a solenoid nested within the magnetic shields, thereby splitting the peak into three distinct sub-peaks by the Zeeman effect. The peaks are distinctly shifted to one side, as predicted due to optical pumping effects [21]. Contrast for this resonance when the B-field is turned to zero is about 7.9 percent. This resonance was produced with the VCSEL at modulation index of about 1.8.

### 3.4 Relative intensity noise measurements

A current topic of significant interest surrounding CPT clocks is the amount by which noise increases when a VCSEL is tuned to resonance. Studies have shown that this effect may be quite significant, with a noise increase of several orders of magnitude [17, 18].

We tested this effect by measuring relative intensity noise (RIN) as a function of frequency. This is defined

$$\text{RIN}(\nu) = N(\nu)/V_0 \tag{3.14}$$

where, if a DC signal is being analyzed,  $N(\nu)$  is the amplitude of the noise component detected in the DC signal at frequency  $\nu$ , and  $V_0$  is the amplitude of the DC signal.

#### 3.4.1 Theory

Camparo writes that transmission noise in a laser when it is tuned to an atomic resonance increases due to efficient conversion of phase modulation (PM) to amplitude modulation (AM) under conditions of resonance [17]. This may be understood in part due to the fact that PM-AM conversion is inevitable whenever intensity is a

varying function with respect to frequency. (See for instance, the way in which the frequency modulation turns into intensity modulation in section 3.2.1 of the lock-in amplifier discussion.) However, it is incorrect to regard this simply as a result of a passive intensity-frequency relationship in an optically thick medium; one must consider the process as an active process. Figure 3.21 shows how this effect works. This

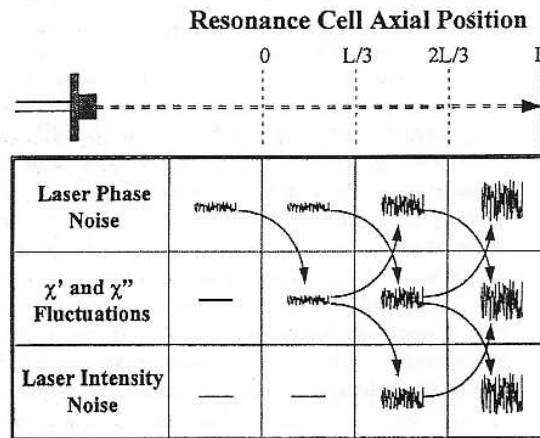


Figure 3.21: Illustration of PM-AM conversion process. As depicted, small fluctuations in phase may be amplified greatly and converted into intensity noise in a nonlinear process as an electromagnetic wave propagates through an optically thick atomic vapor [17].

is a nonlinear process, and hence it has the potential to amplify and convert phase fluctuations by orders of magnitude, thereby significantly degrading the stability of a clock.

### 3.4.2 RIN findings

We tested the importance of this effect with the Kernco VCSEL using the experimental setup shown in figure 3.22.

The primary difference between this and all previous setups is the replacement of the oscilloscope monitoring transmission with a spectrum analyzer. Recording the noise profile of a locked signal, and dividing by the DC output being analyzed,

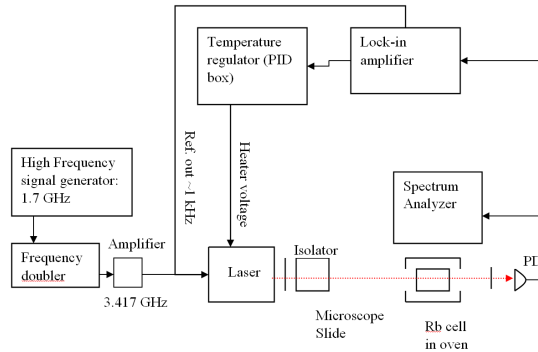


Figure 3.22: Experimental configuration for RIN measurements. All of the setup which also existed for locking with high frequency modulation was used here in the same way as before. In contrast to the setup used to measure EIT, the HF signal generator was on, but not set to frequency modulate. An EIT contrast of about 8 percent allowed us to easily tell when EIT was on or off resonance, and we performed noise tests under both conditions.

we obtained the RIN. We ran tests for the VCSEL signal locked to resonance, locked slightly off resonance ( $\pm 85$  MHz), floating far off resonance, and floating about at resonance but with the rubidium cell removed from the setup. We used the method and calibration described section 3.2.4 to lock to the points at resonance  $\pm 85$  MHz. Two complete sets of results were obtained, taken under slightly different conditions. They are displayed in figures 3.23a and 3.23b.

There was no difference in noise depending on whether the two-photon detuning of the laser was tuned to EIT or not, implying that EIT plays little role in the degree to which laser noise is observed. In the second measurement, there was also no difference between the results when the laser was tuned far off resonance and those when the laser was tuned close to resonance with the cell removed. This implies that the cell windows contribute to noise by a negligible amount. In both measurements, RIN on resonance is greater than RIN far off resonance, and RIN slightly off resonance is greater yet than RIN on resonance. This is qualitatively in accordance with what is expected.

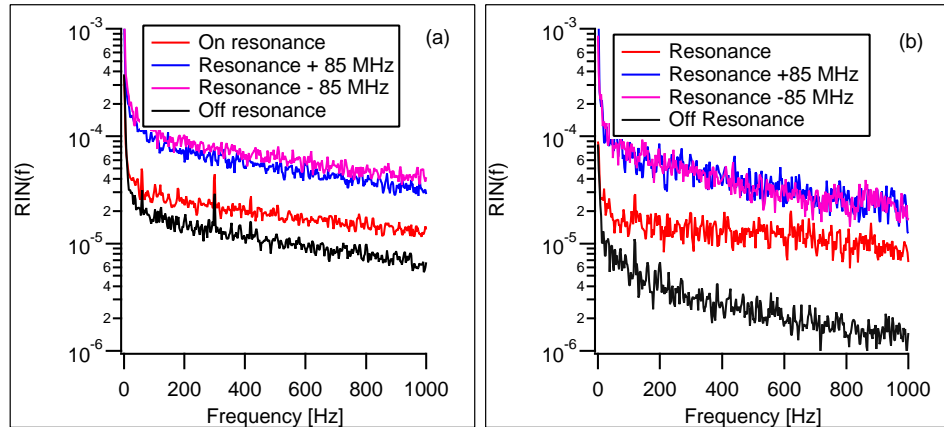


Figure 3.23: Relative intensity noise (RIN) as a function of frequency. The two tests above reflect two different testing situations. In (a) part of the signal from the photodetector was sent to an oscilloscope using a Tee connector, which added noise to the system. The measurements in (b) were taken without the Tee. In both charts, the two top lines (magenta and blue) are at resonance  $\pm 85$  MHz, the middle line (red) is directly on resonance, and the bottom line (black) is off resonance.

There was a noticeable difference in the overall noise between the two tests. This is most likely due to the fact that under the first set of measurements, part of the signal sent to the spectrum analyzer was sent to the oscilloscope using a Tee connector. This connection increased noise considerably. However, if the difference between the off-resonant RIN profile for the second test and the off-resonant profile for the first test is subtracted from all the RIN profiles of the first test, the discrepancy vanishes (see figure 3.24). This is consistent with the hypothesis that a fixed amount of noise was added to the photodetector signal after noise amplification by PM-AM conversion.

If the extra noise shown in the on-resonance and slightly off-resonance profiles above is strictly due to amplification of the baseline noise, then the data suggest that when the laser is locked directly on resonance, noise is amplified by a factor of 3 to 6, and if the laser is locked  $\pm 85$  MHz away from resonance, noise is amplified

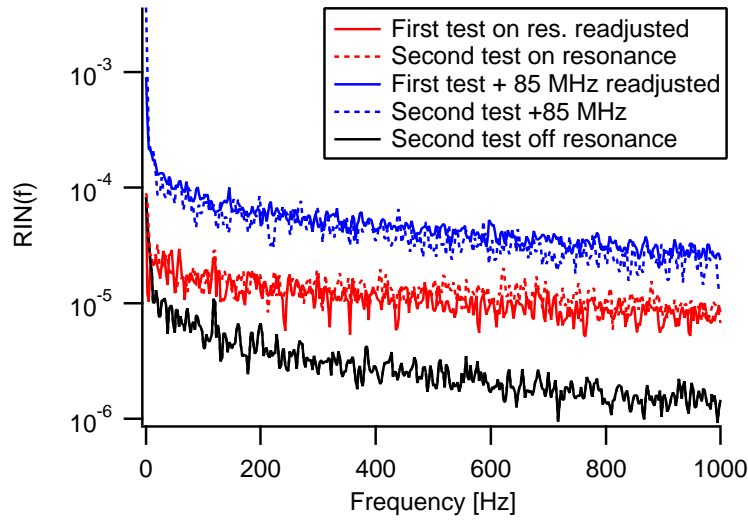


Figure 3.24: The data from figure 3.23a, plotted here as solid lines, is renormalized by subtracting the difference between the off-resonance lines in 3.23a and 3.23b. The result matches very well with data from 3.23a, plotted as hashed lines.

by 1 to 2 orders of magnitude.

### 3.5 Sideband comparison measurements

Sideband amplitude values are a critical part of VCSEL performance. Under conditions of pure phase modulation, the two first-order sideband intensities are equal. This is also true under conditions of pure amplitude modulation. However, if the two are mixed, the first-order sidebands will be of different amplitudes because sidebands from phase modulation are 180 degrees out of phase and sidebands from amplitude modulation are in phase.

The amplitudes of the VCSEL sidebands may be inferred by looking at the heights of resonance peaks as the length of the Fabry-Perot cavity is swept. However, there may be hysteresis in the piezo element of the cavity, or there may be other effects that contribute to error. For this reason we explored an alternative method

of measuring the sidebands.

### 3.5.1 Experimental setup

Besides calculating sidebands by examining the laser line shape through the Fabry-Perot cavity, we measured them by examining a beat note signal using the experimental setup described in figure 3.25.

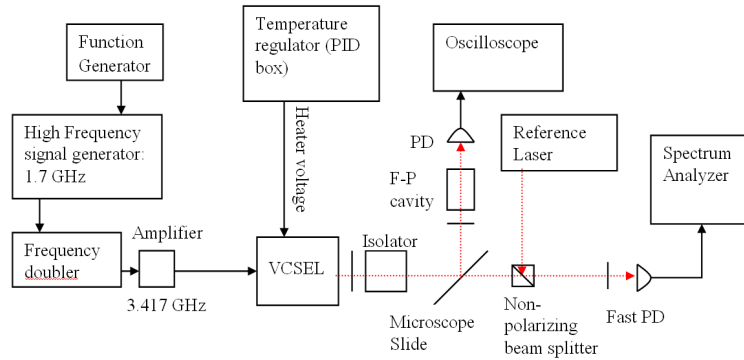


Figure 3.25: Experimental configuration for comparing Fabry-Perot cavity and beat note methods of measuring sideband amplitudes.

Instead of sending the laser through a signal cell, it was merged with a reference laser and sent to the input of a fast photodetector. If  $E_V = \mathcal{E}_V \cos[\omega_V t + \phi(t)]$  is the VCSEL output, and  $E_{ref} = \mathcal{E}_{ref} \cos(\omega_{ref} t)$  is the reference laser output (where an extra noise term  $\phi(t)$  is included in the VCSEL signal but not in the reference laser signal because the linewidth of the reference laser is considerably narrower than that of the VCSEL), then the composite signal intensity detected by the photodetector will be

$$I = (E_V + E_{ref})^2 = E_V^2 + E_{ref}^2 + 2\mathcal{E}_V\mathcal{E}_{ref} \cos[\omega_V t + \phi(t)] \cos(\omega_{ref} t). \quad (3.15)$$

The first two terms of the above equation will be detected by the fast photodetector as a DC signal because they oscillate at optical frequencies. Using a trigonometric identity on the third term, we obtain

$$2 \cos(a) \cos(b) = \cos(a + b) + \cos(a - b) \quad (3.16)$$

$$\Rightarrow I_{beat} \equiv 2\mathcal{E}_V \mathcal{E}_{ref} \cos[\omega_V t + \phi(t)] \cos(\omega_{ref} t) \quad (3.17)$$

$$= \mathcal{E}_V \mathcal{E}_{ref} \cos[(\omega_V - \omega_{ref})t + \phi(t)] \quad (3.18)$$

$$+ \mathcal{E}_V \mathcal{E}_{ref} \cos[(\omega_V + \omega_{ref})t + \phi(t)]. \quad (3.19)$$

The second part of this identity averages out to a DC signal because it oscillates at an optical frequency as well. However, the first term may be adjusted to oscillate quite slowly, depending on the frequency difference between the reference laser and the VCSEL. It may then be detected as a beat note on the fast photodetector. The intensity of this beat note is proportional to the amplitude of the VCSEL. In theory, if a beat note is obtained for the upper and lower sidebands of the modulated VCSEL, then the two may be divided by each other to get a ratio between sideband amplitudes:

$$\frac{I_{beat_1}}{I_{beat_2}} = \frac{\mathcal{E}_{V1}}{\mathcal{E}_{V2}}. \quad (3.20)$$

The fast photodetector and spectrum analyzer we used square the input, so taking the ratio of sidebands measured by this method is directly comparable to taking the ratio of sidebands measured using the Fabry-Perot cavity.

### 3.5.2 Results

A typical beat note spectrum and corresponding Fabry-Perot picture are displayed in figure 3.26. Modulation frequency throughout this study was fixed at 3.417 GHz.

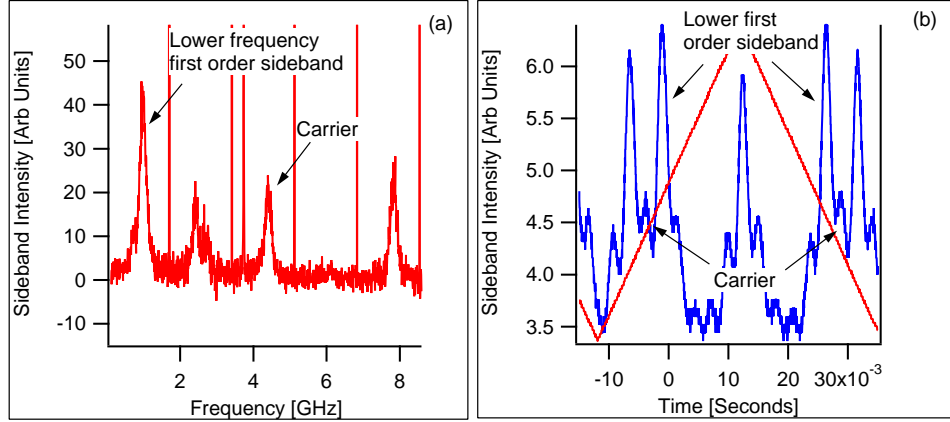


Figure 3.26: Example data traces are shown for sideband calculations using a beat note signal (a) and a Fabry-Perot cavity (b). For (b) the sweep rate is about 130 MHz/second. In both cases, comparisons were made between the low frequency first order sideband and the carrier. In (a) the high frequency sideband at 8 GHz is attenuated by about 1 dB. The sharp spikes are beat note signatures of the VCSEL interfering with itself. Note the evidence of hysteresis in (b), particularly between what should be mirror images of the second order sidebands.

The Fabry-Perot signal displayed some hysteresis depending on whether the piezo element was sweeping up or down in frequency, but the beat note signal was far noisier. Additionally, over time the amplitudes of measured beat frequencies fluctuated considerably, complicating the measurement further.

For a variety of modulation indices we measured ratios between first order sidebands and the carrier, both using data from the Fabry-Perot cavity and from the beat note. We believed fluctuations in beat note amplitude may have been caused by the two beams drifting in and out of alignment over time. In this case, sidebands fluctuate together in time, and the ratio between sidebands is constant. A plot of sideband ratios, as calculated using Fabry-Perot and beat note data, is shown in

figure 3.27. We took most data points shown during a single run on March 22. To check repeatability, we also include four points from a previous data run on March 17. For all points, we kept the beat note frequency at 5 GHz or lower. The fast photodetector we used detects frequencies as high as 12 GHz, but sensitivity attenuates exponentially above 6 GHz.

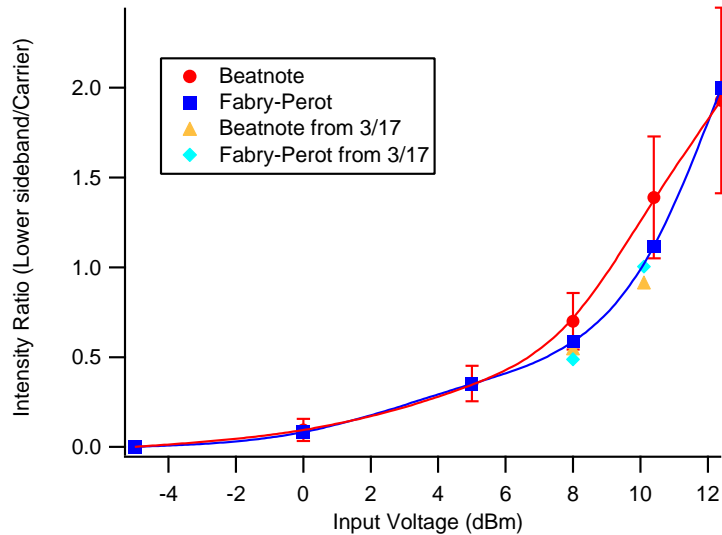


Figure 3.27: Sideband to carrier ratios, as calculated using a Fabry-Perot cavity and a beat note signal. All data, except the four points labeled March 17, is from March 22. The Fabry-Perot cavity calculation (blue squares and diamonds) appears to be the most consistent. Error bars on the March 22 beat note calculation were obtained by looking at noise in the data. Errors for Fabry-Perot calculation are believed to be primarily systematic, and therefore bars are not shown.

Ratios compared between the Fabry-Perot cavity and the beat note setup match very well for small modulation indices. The correlation is poorer at higher modulation indices, as more noise interferes in the beat note signal. The Fabry-Perot cavity points from March 17 match the March 22 data much better than beat note points do. In addition, if we calculate the sidebands using the beat note method, and don't relate sideband intensity to carrier intensity, then the repeatability of the sideband measurement goes down much further.

All of this seems to indicate that the Fabry-Perot cavity method is much better than the beat note analysis method for calculating sideband intensities, and that verification of the accuracy of the Fabry-Perot method by analyzing beat notes is largely unnecessary.

# Chapter 4

## High pressure $N$ -resonance tests

CPT is already a valuable component of small-scale clocks, yielding fractional stabilities lower than  $10^{-12}$  [22–24]. Furthermore, clocks based on CPT have an advantage over more traditional intensity optical pumping (IOP) clocks in that they require no microwave cavity, and thus theoretically can be smaller. The  $N$ -resonance, a far more recent discovery, is only beginning to be explored as a clock reference, but studies thus far have shown it to be promising.

In order to be miniaturized, cells with high buffer gas pressure must be used. Otherwise, atoms will lose coherence too quickly in collisions with cell walls, and the resonance will not be seen [21]. Studies of the  $N$ -resonance under conditions of high buffer gas pressure (40 Torr and 25 Torr) have shown both that shifts may be less significant and that contrast may be stronger for an  $N$ -resonance than for a CPT resonance under similar conditions [10]. In this chapter, we investigate further, repeating the tests under conditions of 100 Torr buffer gas pressure.

## 4.1 Characteristics of interest

We are interested in measuring a few crucial features of a potential clock resonance: light shifts, contrast, and line width. The role of each is described below.

### Light shifts

When an electromagnetic wave is applied to an atomic transition, it produces an AC stark shift, or light shift [25]. In a two-level system, the shift magnitude is given by [26]

$$\Delta_{ls} = -\frac{\Delta}{\gamma_{ab}^2 + 4\Delta^2} |\Omega_P|^2. \quad (4.1)$$

This is a function of detuning  $\Delta$  and field intensity  $|\Omega_P|^2$ , both of which may vary in time. If the laser is phase-modulated, shifts can theoretically be eliminated in a CPT clock with modulation index adjusted to 2.4 [8]. Nonetheless, the dependence has been shown to limit short and medium term frequency stability in CPT clocks [8,23].

### Linewidth and contrast

It is believed that despite the current stability limitations imposed by light shifts and by noise amplification through PM-AM conversion, a properly adjusted rubidium frequency standard will be ultimately limited by photon shot noise in the short term [8]. Stability for such a clock will be given by the following expression in terms of Allen deviation:

$$\sigma(\tau) = \frac{1}{4} \sqrt{\frac{\eta e}{I_{bg}}} \frac{1}{\nu_0} \frac{\Delta\nu}{C} \tau^{-1/2}. \quad (4.2)$$

Here  $\eta$  is photodetector sensitivity (in optical energy per photoelectron),  $e$  is the electron charge,  $I_{bg}$  is the intensity of background absorption light,  $\nu_0$  is atomic reference frequency (6.835 GHz in our case),  $\Delta\nu$  is the full line width of the resonance,

$C \equiv A/I_{bg}$  is contrast, and  $\tau$  is the integration time. Thus, stability will improve as contrast increases and as line width decreases.

## 4.2 Experimental setup

Since the length of the cell we use (1 cm) is smaller than that of the medium-pressure cells used before (7 cm), the temperature of the cell should be higher (80 C). However, at such temperature a leak opened up leading to Rb oxidization. Therefore, we had to operate at somewhat lower temperature (70 C), so the Rb density times the length of the cell was only 50 percent that of the medium pressure cells. For that reason it is impossible to compare the values for the resonance contrast, even though the other measurements (width, light shifts) can be compared.

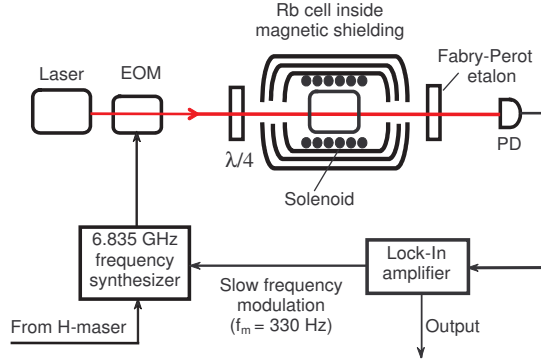


Figure 4.1: Experimental setup for  $N$ -resonance tests. Laser beam diameter inside the cell was 0.8 mm. Optical fields were created using an external cavity diode laser ( $\approx 12$  mW total power) which was then phase modulated at 6.8 GHz with an electro-optic modulator (EOM). Before passing through the cell, the beam was circularly polarized using a quarter-wave plate. The cell was enclosed within three layers of magnetic shielding, and heated with a blown-air oven. It was also centered within a solenoid oriented along the axis of propagation, and a small current was run through the coils, causing the magnetic sublevels of the rubidium transition to separate. After passing through the cell, the beam passed through a quartz, narrow-band Fabry-Perot etalon (FSR = 20 GHz, finesse = 30), and this filtered out everything but the probe frequency. The remaining beam was then detected using a photodetector.

A block diagram of the experimental setup, depicted in figure 4.1 is the same as in reference [10]. A Fabry-Perot etalon filters the light coming out of the cell, allowing only the probe field to impinge upon the photodetector. The photodetector signal could be sent directly to an oscilloscope, yielding information about signal absorption and feature shape. It could also be detected using a lock-in amplifier, as shown in the figure. In the second case, a slowly oscillating reference modulation was applied to the 6.8 GHz signal, and corresponding variations in signal intensity were detected by the lock-in input<sup>1</sup>. When rearranged to form a locked loop, this lock-in output will provide the critical lock point for the clock.

We observed the  $N$ -resonance by first tuning the carrier so that the probe would be close to the D1 transition between the  $F = 2$  ground state and either the  $F' = 1$  or  $F' = 2$  excited states. We then gradually swept the 6.8 GHz modulation frequency while detecting the output transmission with the photodetector. Sweeps were regulated by a computer and usually lasted between 1 and 5 minutes.

### 4.3 Results

A few characteristic shapes of the resonance are displayed in figure 4.2. Here, transmission is displayed as a function of hyperfine frequency detuning. We focused on the  $m_F = 0$  magnetic sublevel (middle resonance). Unlike the other two sublevels, it displays no first-order magnetic field dependence, and is therefore naturally more stable.

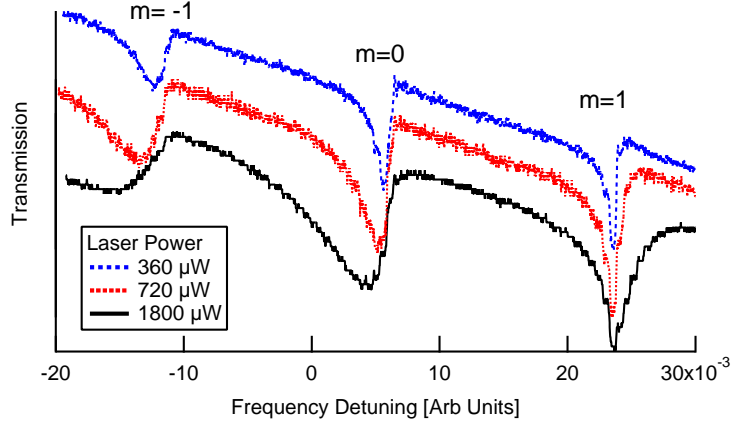


Figure 4.2: Three  $N$ -resonance profiles at different laser intensities. Feature amplitudes have been normalized and backgrounds have been removed to fit the shapes into the plot. The center resonance, corresponding to the  $m_F = 0$  transition, is increasingly asymmetrical at higher laser powers.

### 4.3.1 Light shifts

The frequency shift, while notably different from that predicted by the model in equation (4.1), qualitatively matches the shape of frequency shifts at lower buffer gas pressure [10]. At the local minimum and maximum, linear dependence is zero, so we measured curvature. At  $2 \text{ mHz}/\text{MHz}^2$  for the minimum, and  $-2.6 \text{ mHz}/\text{MHz}^2$  for the maximum, this meets or improves upon the frequency shift for medium pressure buffer gas cells, which was measured at  $2.5 \text{ mHz}/\text{MHz}^2$  for 40 Torr Ne and  $4.0 \text{ mHz}/\text{MHz}^2$  for 25 Torr Ne-Ar mixture [10].

The power shift is somewhat larger than that measured with lower buffer gas pressure, with a linear dependence of  $30 \text{ mHz}/(\mu\text{W}/\text{cm}^2)$ . In both the medium pressure cells the dependence was near  $25 \text{ mHz}/(\mu\text{W}/\text{cm}^2)$ .

---

<sup>1</sup>This method is essentially the same as that employed in section 3.2.1, although this applies to the multiple photon transition whereas that was used to lock the single-photon transition.

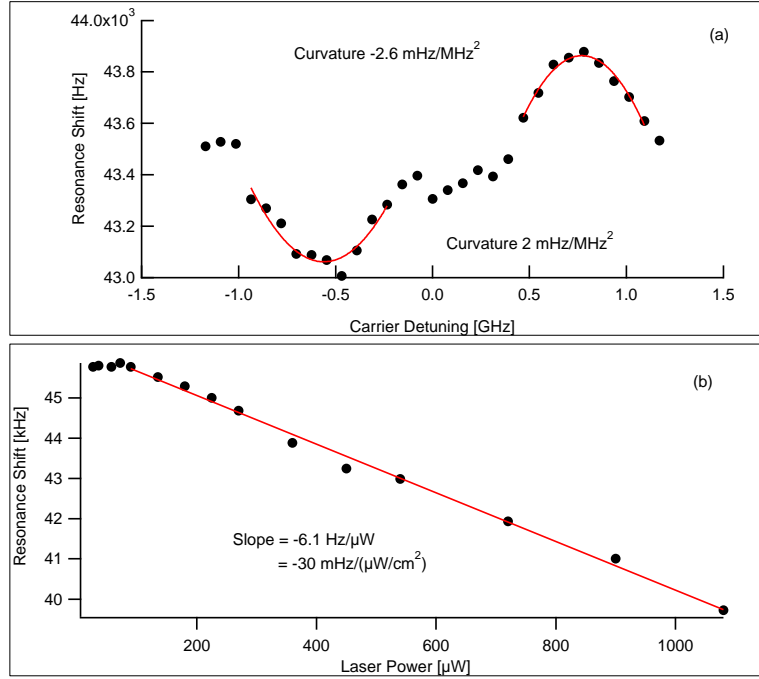


Figure 4.3: Plot of light shift vs. laser detuning and power. Curvature in (a), between 2 and 2.6 mHz/MHz<sup>2</sup>, is less than in reference [10]. In (b) the slope, at 30 mHz/( $\mu\text{W}/\text{cm}^2$ ), is steeper than medium pressure tests [10].

### 4.3.2 Widths

Figure 4.4 shows estimates of line widths. These were calculated by measuring the distance in frequency between the maximum and minimum of the resonance as observed on the lock-in amplifier. If modulation frequency is much less than feature width, this is the frequency difference between the left and right inflection points of a resonance. Then, for a Lorentzian curve:

$$y = \frac{A}{1 + (x/\sigma)^2}, \quad \frac{\partial^2 y}{\partial x^2} = A \left( \frac{8x^2}{\sigma^4(1 + (x/\sigma)^2)^3} - \frac{2}{\sigma^2(1 + (x/\sigma)^2)^2} \right) \quad (4.3)$$

$$\frac{\partial^2 y}{\partial x^2} = 0 \quad \Rightarrow \quad x = \sigma/\sqrt{3} \approx 0.58 \sigma. \quad (4.4)$$

This method of width calculation is particularly useful when laser intensity is very low and signal to noise ratios are good enough for lock-in detection, but not direct absorption detection.

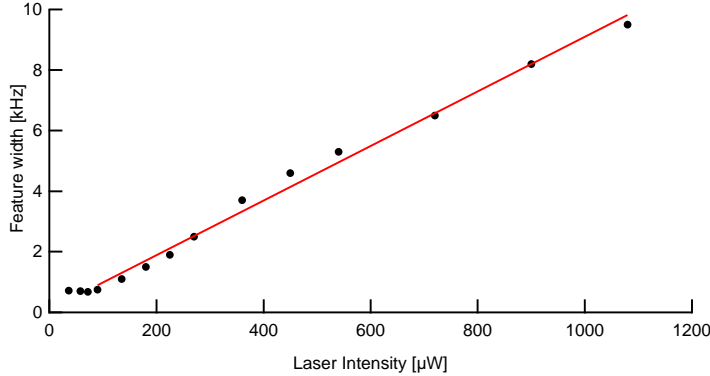


Figure 4.4: Line width with respect to laser power. Widths are slightly wider than those measured for medium buffer gas pressure.

The widths measured above reflect a larger degree of broadening than those measured in the medium pressure tests. Such broadening is not good if the resonance is to be used as a clock resonance; however, studies with another 100 Torr cell under similar conditions imply that contrast for the  $N$ -resonance is not subject to depletion due to optical pumping into end states in the same way that the CPT resonance is [27]. Figure 4.2 shows this as well. Even at large intensity, the  $m_F = 0$  resonance is as pronounced as the  $m_F = 1$  resonance. The two effects will offset each other to some degree.

### 4.3.3 Line shape asymmetry

Both the peculiar broadening and power dependence of the  $m_F = 0$  resonance may be seen in the overall shape of the absorption and lock-in profiles (see figures 4.2 and 4.5). As we increase laser intensity the  $m_F = 0$  resonance not only broadens; it also

becomes increasingly asymmetrical, with a steep slope on the high frequency side and a notch at the point the resonance flattens out, and with a much more gentle slope trailing the resonance off on the low frequency side. As power increases, the position of the notch remains fixed, and it looks as if the resonance is stretched down in frequency, causing the resonance minimum to shift and the line to broaden.

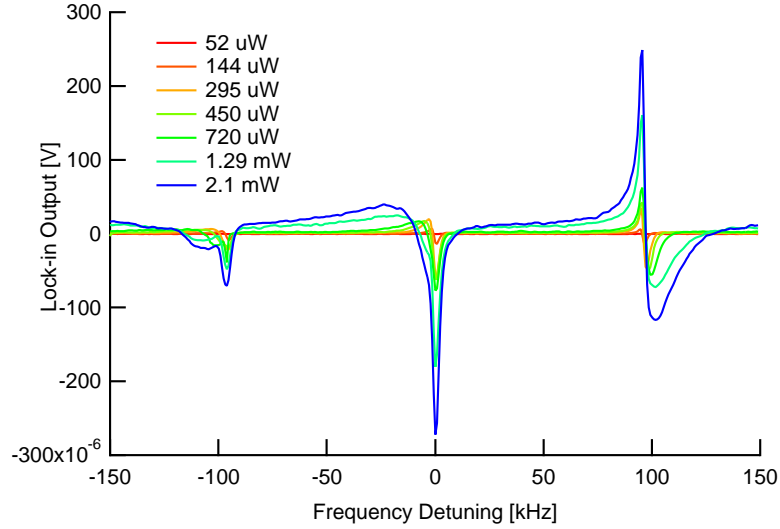


Figure 4.5: Comparison of the lock-in output signals for the  $N$ -resonance at different laser powers. The  $m_F = 1$  zero crossing remains fixed as power increases, but the  $m_F = 0$  crossing does not. Increasing line shape asymmetry may also be observed as laser power is increased.

We note that the  $m_F = 1$  resonance suffers from little of this behavior, and remains symmetric as power is increased. This suggests that the  $N$ -resonance may be well-suited for magnetometry. Because of the Zeeman effect, the  $m_F = 1$  and  $m_F = -1$  resonances exhibit high magnetic sensitivity. Devices have already been constructed based on CPT phenomena that measure fields at the level of picotesla [12].



# Chapter 5

## Further study

Several open questions remain with the immediate experiments performed on the  $N$ -resonance. For instance, the notch on the higher frequency side of the  $m_F = 0$  resonance is relatively fixed as laser power varies. We might try locking to this feature as opposed to the bottom of the resonance. The  $m_F = 1$  transition warrants more study in general, particularly in connection with its possibilities for use as a magnetometer.

More experiments might be done to obtain a better understanding of the VCSEL as well. For instance, the beatnote method of calculating sidebands might be greatly improved by finding a way to phase-lock the VCSEL and reference laser. This would give narrower lines and better signal to noise ratio. A more efficient isolator might be installed in place of the polarizing beam splitter and quarter-wave plate, in order to enhance performance.

The real potential for the future of these experiments lies in using the VCSEL as a working tool. Installing the laser in a setup so that both single and multiple photon transitions can be locked would allow CPT and  $N$ -resonances to be studied in relation to the stability they produce in an actual working clock. The longer-

term prospects for these studies will almost certainly be to install the VCSEL in this setup and compare CPT and other types of resonances by measuring an actual Allen variance, rather than simply using the one inferred by contrast, line width, and light shift characteristics.

# Bibliography

- [1] J. Hafele and R. Keating, *Science* **177**, 168 (1972).
- [2] E. Fortson, D. Kleppner, and N. Ramsey, *Phys. Rev. Lett.* **13**, 22 (1964).
- [3] D. Bear, R. Stoner, R. Walsworth, V. Kostelecky, and C. Lane, *Phys. Rev. Lett.* **85**, 5038 (2000), *ibid.* **89**, 209902(E) (2002).
- [4] E. Fortson, private communication.
- [5] NIST F1: Cesium fountain atomic clock, (Accessed 2005), <http://tf.nist.gov/cesium/fountain.htm>.
- [6] Microclocks at NIST: Applications, (Accessed 2005), <http://tf.nist.gov/ofm/smallclock/Applications.htm>.
- [7] J. Vig, *IEEE Trans. on Ultrasonics, Ferroelectrics, and Frequency Control* **40**, 522 (1993).
- [8] J. Vanier, M. Levine, D. Janssen, and M. Delaney, *IEEE Trans. Instrum. Meas.* **52**, 822 (2003).
- [9] A. Zibrov, C. Ye, Y. Rostovtsev, A. Matsko, and M. Scully, *Phys. Rev. A* **65**, 043817 (2002).

- [10] S. Zibrov, I. Novikova, D. Phillips, A. Taichenachev, V. Yudin, R. Walsworth, and A. Zibrov, (Submitted to Phys. Rev. A) e-Print archive physics/0501090 (2005), <http://www.arxiv.org/abs/physics/0501090>.
- [11] R. Wynands and A. Nagel, Appl. Phys. B **68**, 1 (1999), *ibid.* **70**, 315 (2000).
- [12] M. Stahler, S. Knappe, C. Affolderbach, W. Kemp, and R. Wynands, Europhys. Lett. **54**, 323 (2001).
- [13] M. O. Scully and M. S. Zubairy, *Quantum Optics* (Cambridge University Press, Cambridge, 1997).
- [14] Appendix A: Interaction of electromagnetic fields with two-level atoms; and the linear Faraday effect, Slow light lab bench notes, Harvard Physics course 191r: Advanced laboratory, 2004.
- [15] G. Alzetta, A. Gozzini, L. Moi, and G. Orriols, Nuovo Cimento B **36**, 5 (1976).
- [16] K.-J. Boller, A. Imamoglu, and S. Harris, Phys. Rev. Lett. **66**, 2593 (1991).
- [17] J. Camparo and W. Buell, Proc. IEEE Int. Freq. Cont. Symp. 253 (1997).
- [18] J. Camparo, J. Opt. Soc. Am. B **15**, 1177 (1998).
- [19] G. Bjorklund, Optics Letters **5**, 15 (1980).
- [20] J. Moore, C. Davis, and M. Coplan, *Building Scientific Apparatus* (Perseus Books, Cambridge, MA, 2003).
- [21] Y.-Y. Jau, A. Post, N. Kuzma, A. Braun, M. Romalis, and W. Happer, Phys. Rev. Lett. **92**, 110801 (2004).

- [22] S. Knappe, R. Wynands, J. Kitching, H. Robinson, and L. Hollberg, *J. Opt. Soc. Am. B* **18**, 1545 (2001).
- [23] M. Merimaa, T. Lindwall, I. Tittonen, and E. Ikonen, *J. Opt. Soc. Am. B* **20**, 273 (2003).
- [24] J. Vanier, M. Levine, S. Kendig, D. Janssen, C. Everson, and M. Delaney, *Int. Freq. Control Symposium* (2004).
- [25] B. Mathur, H. Tang, and W. Happer, *Phys. Rev.* **171**, 11 (1968).
- [26] J. Vanier and C. Audoin, *The Quantum Physics of Atomic Frequency Standards* (Adam Hilger, Bristol, U.K., 1989).
- [27] I. Novikova, private communication.

# Appendix A

## Technical data on the Kernco SN: 61-39 VCSEL

We include here a reproduction of the specifications provided by Kernco of the SN: 61-39 VCSEL. The laser comes from a series of VCSELs that Kernco uses in its atomic clocks. Laser wavelength is not listed in the specifications, but it is tuned to roughly 795 nm, the D1 transition line of rubidium.

Kernco Inc.  
22 July, 2004

LASER SN: 61-39

Information on Laser:

1. Optical power: 216 uW
2. Required RF modulation frequency: 3.417GHz
3. Required RF power: +3.5dBm
4. Laser will be at wavelength when  $Rt2 \approx 1.7V$ .
5. Do NOT heat the laser over 80C ( $Rt2 = 1.5V$ ).
6. Kernco suggests using a servo heating control rather than manual control.

Laser board pin out:

- 1= +5 Volts +/- 0.5V
- 2=  $Rt1$  (2.8V at 20C to 1.5V at approx. 80C. DO NOT EXCEED 80C)
- 3=  $Rt2$  (100k at 20C)
- 4= Laser Heater Return
- 5= Laser Heater (no more than 3.7V should be required)
- 6= Ground
- 7= Ground
- 8= Ground
- 9= n/c

Part No.	Value	Notes
00001	100k	
00002	100k	
00003	100k	
00004	100k	
00005	100k	
00006	100k	
00007	100k	
00008	100k	
00009	100k	
00010	100k	
00011	100k	
00012	100k	
00013	100k	
00014	100k	
00015	100k	
00016	100k	
00017	100k	
00018	100k	
00019	100k	
00020	100k	
00021	100k	
00022	100k	
00023	100k	
00024	100k	
00025	100k	
00026	100k	
00027	100k	
00028	100k	
00029	100k	
00030	100k	
00031	100k	
00032	100k	
00033	100k	
00034	100k	
00035	100k	
00036	100k	
00037	100k	
00038	100k	
00039	100k	
00040	100k	
00041	100k	
00042	100k	
00043	100k	
00044	100k	
00045	100k	
00046	100k	
00047	100k	
00048	100k	
00049	100k	
00050	100k	
00051	100k	
00052	100k	
00053	100k	
00054	100k	
00055	100k	
00056	100k	
00057	100k	
00058	100k	
00059	100k	
00060	100k	
00061	100k	
00062	100k	
00063	100k	
00064	100k	
00065	100k	
00066	100k	
00067	100k	
00068	100k	
00069	100k	
00070	100k	
00071	100k	
00072	100k	
00073	100k	
00074	100k	
00075	100k	
00076	100k	
00077	100k	
00078	100k	
00079	100k	
00080	100k	
00081	100k	
00082	100k	
00083	100k	
00084	100k	
00085	100k	
00086	100k	
00087	100k	
00088	100k	
00089	100k	
00090	100k	
00091	100k	
00092	100k	
00093	100k	
00094	100k	
00095	100k	
00096	100k	
00097	100k	
00098	100k	
00099	100k	
00100	100k	

Monitor Thermistor Readings

Rt1 will read in Volts and should NOT go below 1.5V

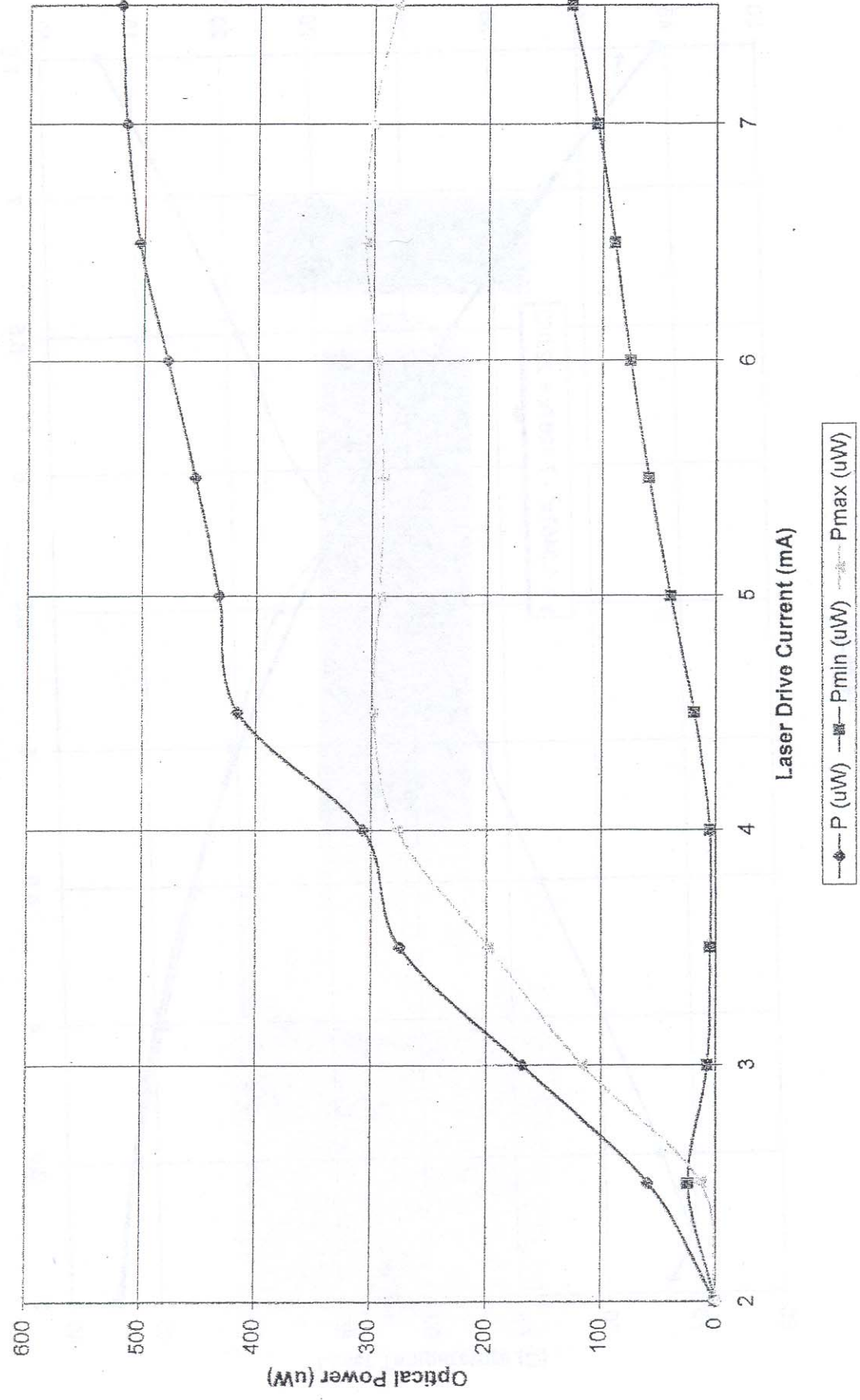
Rt2 will read in Ohms and should NOT go below 10kOhm

TEMP. (C)	Rt1 (V)	Rt2 (Ohms)
26.10	2.714	95000
37.86	2.545	56000
40.49	2.500	50000
41.44	2.483	48000
42.44	2.464	46000
43.49	2.444	44000
44.60	2.423	42000
45.77	2.400	40000
47.00	2.375	38000
48.31	2.348	36000
49.71	2.318	34000
51.20	2.286	32000
52.80	2.250	30000
54.53	2.211	28000
56.40	2.167	26000
58.44	2.118	24000
60.69	2.063	22000
63.18	2.000	20000
65.97	1.929	18000
69.13	1.846	16000
72.79	1.750	14000
77.09	1.636	12000
82.30	1.500	10000
88.87	1.333	8000
97.66	1.125	6000

Danvers, MA 01923  
Tel: (978) 777-1956  
Fax: (978) 777-1958  
www.kernco.com

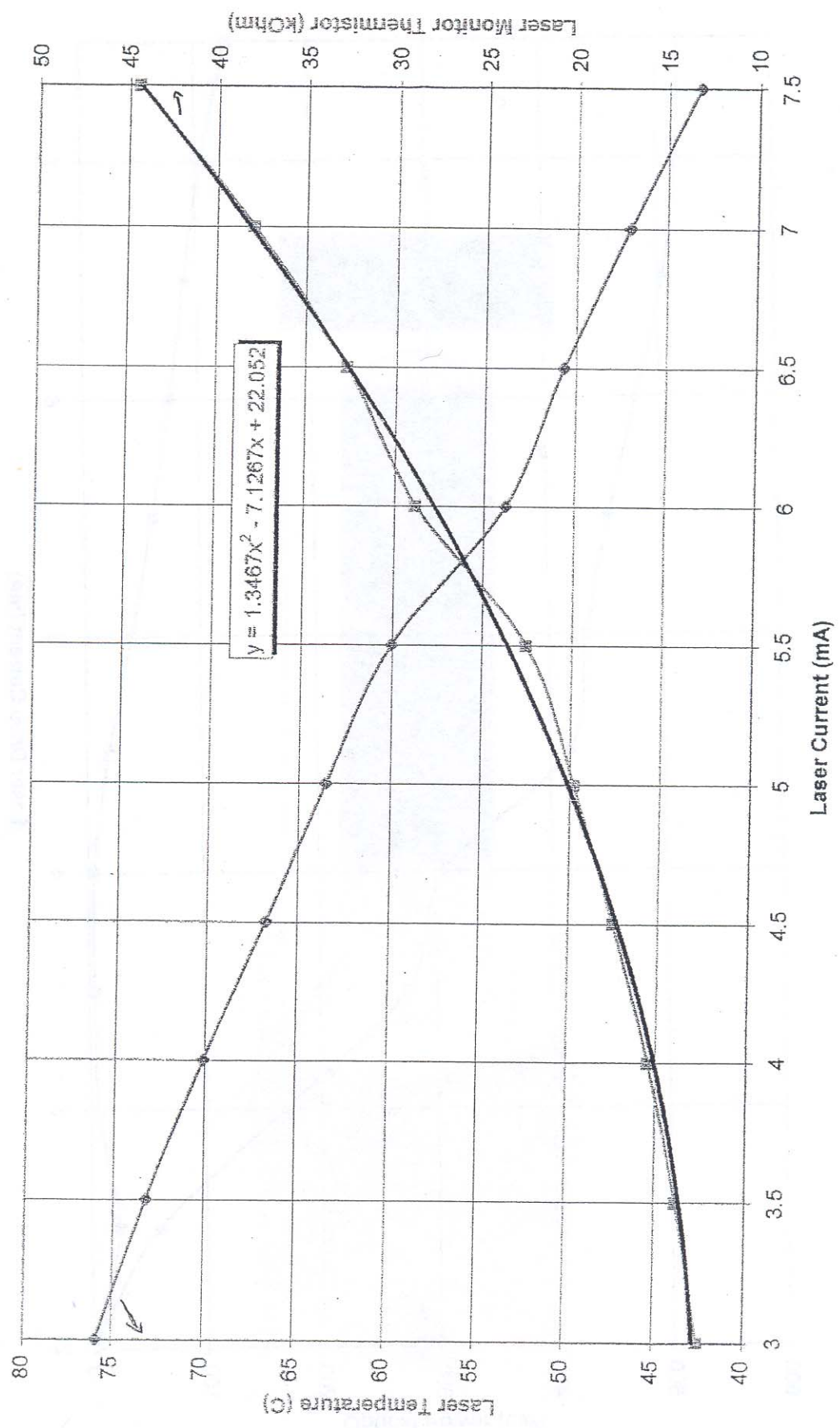


Laser 61-39 Optical Power Vs Laser Drive Current.  
Laser at ~80C. 11/07/03



Tested by Adam Laiacano

Laser 61-39  
 Points Where Laser Operates at 794nm.  
 11-07-03



Modulation index of 1.8 at 3.417GHz.  
+3.5dBm RF Power Supplied to Laser.

